

RESEARCH ARTICLE

10.1002/2013JC009724

An intercomparison of Arctic ice drift products to deduce uncertainty estimates

Hiroshi Sumata¹, Thomas Lavergne², Fanny Girard-Ardhuin³, Noriaki Kimura⁴, Mark A. Tschudi⁵, Frank Kauker^{1,6}, Michael Karcher^{1,6}, and Rüdiger Gerdes^{1,7}

Key Points:

- Ice drift products from four different institutions were compared
- Difference of drift vectors is covariant with ice concentration and thickness
- Present study provides uncertainty estimates for ice drift products

Correspondence to:

H. Sumata,
hiroshi.sumata@awi.de

Citation:

Sumata, H., T. Lavergne, F. Girard-Ardhuin, N. Kimura, M. A. Tschudi, F. Kauker, M. Karcher, and R. Gerdes (2014), An intercomparison of Arctic ice drift products to deduce uncertainty estimates, *J. Geophys. Res. Oceans*, 119, 4887–4921, doi:10.1002/2013JC009724.

Received 11 DEC 2013

Accepted 14 JUL 2014

Accepted article online 16 JUL 2014

Published online 8 AUG 2014

Corrected 29 DEC 2014

This article was corrected on 29 DEC 2014. See the end of the full text for details.

¹Alfred Wegener Institute, Helmholtz Centre for Polar and Marine Research, Bremerhaven, Germany, ²Norwegian Meteorological Institute, Oslo, Norway, ³Laboratory of Oceanography from Space, Ifremer, Plouzane, France, ⁴National Institute of Polar Research, Tachikawa, Japan, ⁵University of Colorado, Boulder, Colorado, USA, ⁶Ocean Atmosphere Systems, Hamburg, Germany, ⁷Jacobs University, Bremen, Germany

Abstract An intercomparison of four low-resolution remotely sensed ice-drift products in the Arctic Ocean is presented. The purpose of the study is to examine the uncertainty in space and time of these different drift products. The comparison is based on monthly mean ice drifts from October 2002 to December 2006. The ice drifts were also compared with available buoy data. The result shows that the differences of the drift vectors are not spatially uniform, but are covariant with ice concentration and thickness. In high (low) ice-concentration areas, the differences are small (large), and in thick (thin) ice-thickness areas, the differences are small (large). A comparison with the drift deduced from buoys reveals that the error of the drift speed depends on the magnitude of the drift speed: larger drift speeds have larger errors. Based on the intercomparison of the products and comparison with buoy data, uncertainties of the monthly mean drift are estimated. The estimated uncertainty maps reasonably reflect the difference between the products in relation to ice concentration and the bias from the buoy drift in relation to drift speed. Examinations of distinctive features of Arctic sea ice motion demonstrate that the transpolar drift speed differs among the products by 13% (0.32 cm s^{-1}) on average, and ice drift curl in the Amerasian Basin differs by up to 24% ($3.3 \times 10^4 \text{ m}^2 \text{ s}^{-1}$). These uncertainties should be taken into account if these products are used, particularly for model validation and data assimilation within the Arctic.

1. Introduction

Low-resolution remotely sensed sea ice drift products are widely used for validation of coupled ocean-sea ice models [Kreyscher *et al.*, 2000; Martin and Gerdes, 2007], model parameter estimation [Tremblay and Hakakian, 2006; Miller *et al.*, 2006; Nguyen *et al.*, 2011], and data assimilation in the Arctic Ocean [Stark *et al.*, 2008; Rollenhausen *et al.*, 2009; Sakov *et al.*, 2012] together with ice concentration and ice thickness products. A variety of ice drift products, which are obtained from different satellite-borne sensors, different time intervals for detecting ice motion, and/or different algorithms for deriving drift vectors, are available [e.g., Kwok *et al.*, 1998; Fowler, 2003; Lavergne *et al.*, 2010; Girard-Ardhuin and Ezraty, 2012]. The advantages of such products in comparison with in situ data are an Arctic-wide spatial coverage with a constant time interval and gridded data format, which makes the products easily suitable for evaluating the model-observation misfit of basin-scale sea-ice simulations.

For a systematic evaluation of the model-observation misfit, one needs to specify the uncertainty of the respective data, since the cost function measuring the misfit is usually defined by the square of the difference between modeled and observed quantities, normalized by the square of the corresponding uncertainties [e.g., Menke, 1989]. In many ice-drift products, however, uncertainty is not provided as a function of space and time, but rather as a constant value, inferred from the study of the comparison with buoys. In that respect, ice-motion products are similar to many remote-sensing products that do not distribute time-space varying maps of uncertainties along with the main geophysical variable they characterize. Only a handful of products and algorithms so far reached a mature enough state for designing and applying a specific algorithm to derive their uncertainties. Incidentally, the alternative approach to achieve time-space varying uncertainties from a large data set of observed validation data is not possible for sea-ice motion, since the number of in situ observations is still limited and is not sufficient to cover the entire spatial and temporal variability of the Arctic Ocean.

The in situ measurements of ice drift are mostly achieved by tracking positions of buoys [Ortmeyer and Rigor, 2004], which, however, seldom cover the shelves and continental slope areas. Due to the severe ice conditions of the Arctic Ocean, it is a demanding task to increase the number of platforms to cover the entire Arctic Ocean with sufficient density, and this will probably hold for the future. In addition, it is also a difficult task to estimate a global uncertainty for satellite-based data sets through the comparison with point measurements as references, since the direct measurements by buoys provide local information whereas satellites measure ice motion over a much larger area. Since realistic estimates of uncertainties based on validation through direct observations is quite difficult on the scale of the Arctic Ocean, data producers should feel encouraged to design uncertainty algorithms associated to their motion tracking methodologies.

In the absence of such uncertainty maps, an intercomparison of drift products to assess the spatial and temporal differences among the products, can be utilized as an estimate of the uncertainty of the data although this uncertainty might not be equivalent to an error estimate. Ice drift products are necessary for sea-ice model validation, albeit only a few studies have focused on differences among the products [e.g., Martin and Gerdes, 2007; Hwang and Lavergne, 2010; Rozman et al., 2011]. Martin and Gerdes [2007] compared monthly mean ice drift product from the National Snow and Ice Data Center (NSIDC) [Fowler, 2003] with that from Centre ERS d'Archivage et de Traitement (CERSAT) [Girard-Arduin and Ezraty, 2012] for model validation purpose. They showed that the spatial patterns of ice drift are similar in the two products, whereas the modal ice speeds and speed distribution show some differences in autumn. Hwang and Lavergne [2010] examined the difference in six drift products from the Ocean and Sea Ice Satellite Application Facility (OSI SAF) and CERSAT by a comparison with ice drift from buoys. They found that drift products using higher resolution images and/or the Continuous Maximum Cross Correlation (CMCC) method yield better error statistics than ones using lower resolution images and/or the Maximum Cross Correlation (MCC) method. They also pointed out the necessity for further analyses including more validation data.

Another example is the comparison of the products (CERSAT, OSI SAF, advanced synthetic aperture radar and moored acoustic Doppler current profilers) in the Laptev Sea area made by Rozman et al. [2011]. They compared satellite-derived and in situ measured ice drift for a validation of modeled ice drift. They concluded that the CERSAT product in the Laptev Sea has a strong correlation with in situ measurement and lower root mean square differences (RMSD) compared to the OSI SAF product, and recommended using more than one satellite product for model validation because of the differences between the products. As shown in these studies, ice drift obtained from different sensors, different time intervals, and different algorithms potentially have contrasting features, and different advantages and weaknesses depending on their usage and application. Examining such differences can provide practical and useful information for users.

The aim of this study is to clarify the differences among the products and utilize the differences as a measure of uncertainty, which can be applied to sea-ice model validation and data assimilation. Particularly, we focus on Eulerian-based uncertainty estimates for validation and data assimilation of medium resolution sea ice models (~50 km horizontal grid spacing), a resolution of which is typical for recent IPCC models. For this purpose, we make an intercomparison between remotely sensed ice-drift products in the Arctic Ocean and additional comparisons of these products with ice drift obtained from buoy observations. We also calculate uncertainty estimates based on the comparison results. We compare four different products; low-resolution sea ice drift [Lavergne and Eastwood, 2010] provided from OSISAF, sea ice drift in the central Arctic by an enhanced combination of scatterometer and radiometer [Girard-Arduin and Ezraty, 2012] from CERSAT, ice drift vectors from Kimura et al. [2013] at University of Tokyo, and Polar Pathfinder Daily 25 km EASE-Grid Sea Ice Motion Vectors, Version 2 [Tschudi et al., 2010; Fowler et al., 2013] from NSIDC. In addition to the above products, we also utilize interpolated ice velocity fields and half-daily buoy positions [Ortmeyer and Rigor, 2004] from the International Arctic Buoy Programme (IABP). Based on the comparisons between these products, we present Eulerian-based uncertainty estimates for the respective products as a function of ice concentration and ice-drift speed.

We compare monthly mean ice drift inferred from the products from September 2002 to December 2006. One of the reasons for using monthly mean drift is that time-averaged vectors are favorable to exclude noisy short-timescale variation and to capture approximate features of seasonal and spatial variations of sea-ice motion. Such monthly means are commonly used for validation of coupled sea ice-ocean models [e.g., Martin and Gerdes, 2007] and for model parameter optimization [Miller et al., 2006; Sumata et al., 2013].

Table 1. Gridded Ice Drift Products Used for Comparison

Product Name	Original Data	Algorithm	Drift Estimation Interval	Spatial Resolution	Period	Summer Data
OSI SAF ^a	AMSR-E (37GHz)	CMCC	2 days	62.5 km	2002–2006	No
CERSAT ^b	QuikSCAT or ASCAT, SSM/I (85GHz)	MCC	6 days + 3 days	62.5 km	2009 – 1991	No
KIMURA ^c	AMSR-E (winter:89GHz, summer: 18.7 GHz)	Improved MCC	1 day	winter:37.5 km, summer:75.0 km	2003–2011	Yes
NSIDC ^d	Buoy position, AVHRR, SMMR(37 GHz), SSM/I(87 GHz), AMSR-E(39, 90GHz)	MCC + Cokriging method	1 day	25.0 km	1978–2012	Yes
IABP/D ^e	Buoy position	Optimal interpolation	12 h	~ 100 km	1979–2011	Yes

^aOSI-405 Low-resolution ice drift product [Lavergne and Eastwood, 2010].

^bSea ice drift in the central Arctic combining QuikSCAT and SSM/I sea ice drift data [Girard-Arduin and Ezraty, 2012].

^cKimura et al., [2013].

^dPolar pathfinder daily 25 km EASE-Grid sea ice motion vectors, Version 2 [Fowler et al., 2013].

^eInterpolated ice velocity fields [Thorndike et al., 1983; Colony and Rigor, 1989].

Another reason is that the time intervals chosen to calculate drift vectors from a pair of remotely sensed images are different among the products from 1 to 6 day lags and therefore we have to standardize the temporal representativeness of the data. The 2002–2006 period is the longest time window with overlapping data coverage of the four different products employed. It should be noted that in all ice-drift products the methods are based on the detection of ice displacement between two reference times, and therefore they do not provide any direct information regarding instantaneous or mean ice velocity. In this study, we use the term “ice drift velocity” defined by the displacement divided by the time interval between the reference times of the products. Note that this definition of “velocity” ignores velocity components associated with ice motion fluctuations on shorter timescales than the interval between the reference times.

The paper is organized as follows: section 2 describes the data products and the processing of the data, section 3 provides the intercomparison results including a comparison with buoy data and uncertainty estimates. The paper ends with a summary and discussion in section 4.

2. Data

In this section, we provide descriptions of the ice drift products (see Table 1) and other data sets used in this study (buoy position, ice concentration, and ice thickness).

2.1. OSISAF Product

We utilize the low-resolution sea ice drift product OSI-405 [Lavergne and Eastwood, 2010] from the European Organization for the Exploitation of Meteorological Satellites (EUMETSAT) OSISAF. The data for the comparison period (2002–2006) are a single sensor product derived from the Advanced Microwave Scanning Radiometer of the Earth Observation System (AMSR-E). A distinctive feature of the product is that a sequence of remotely sensed images is processed by the CMCC method, which builds on the MCC method but relies on a continuous optimization step for computing the motion vector [Lavergne et al., 2010]. An advantage of the method is to efficiently attenuate the quantization noise inherent to the MCC method. Although OSISAF provides other kinds of drift products, we refer to this product as OSISAF to discriminate from the other products used here. The data set gives positions of ice “parcels” before and after a certain time interval (48 h) as daily files from January to April and from October to December with some data gaps. The initial position of the “parcels” is fixed to the grid points defined on the polar stereographic coordinate with a 62.5 km parcel size, while the position of the parcels after the time interval is provided as ice displacement data. The data set also contains rejection and quality index flags, which can be used for the user’s post processing purposes.

For the comparison, we first calculated monthly mean ice drift vectors from the daily files. In this process, we adopted data values whose quality index flag is “nominal_quality.” We defined a monthly mean drift at a data point, if the number of the drift data is greater or equal to 90% of the full temporal coverage of the

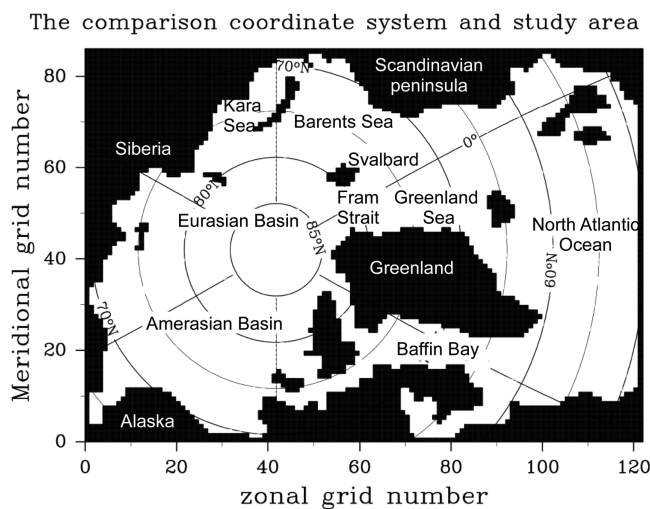


Figure 1. The study domain with major topographic features cited in the text. The horizontal resolution of the comparison grid is visible by the coastline.

corresponding month. Second, the monthly mean drift vectors are projected from the original data coordinate to a coordinate system employed for the comparison with a maximum interpolation distance of 45 km (hereafter referred to as comparison grid). The comparison coordinate system is formulated on a spherical rotated grid of the Earth, whose geographical north pole is shifted to 60°E on the equator. The horizontal resolution is 54.8 km × 54.8 km (Figure 1). The coordinate system offers nearly equidistant grid cells in the Arctic Ocean. It is incidentally

the coordinate system used for running simulations of the North Atlantic-Arctic Ocean Sea Ice Model (NAO-SIM) [Kauker et al., 2009, Sumata et al., 2013]. The monthly mean data cover the entire Arctic Ocean from October 2002 to December 2006 except the summer months (from May to September).

2.2. CERSAT Product

Institut Français de Recherche pour l'Exploitation de la Mer (Ifremer)/CERSAT provides a number of ice drift products obtained from different sensors, different time intervals, and different combinations of single-sensor products as described in Girard-Arduin and Ezraty [2012]. The products have been widely used in modeling and data assimilation studies [e.g., Martin and Gerdes, 2007; Rollenhagen et al., 2009; Sakov et al., 2012] and contributed to the progress of sea ice modeling in the Arctic Ocean. In the present comparison, we employed the Lagrangian monthly aggregated ice drift product combining QuikSCAT and SSM/I products [Girard-Arduin and Ezraty, 2012] (hereafter referred to as CERSAT). The algorithm used to derive ice drift from backscatter and brightness temperature maps is based on the MCC method applied on the Lagrangian field [Girard-Arduin and Ezraty, 2012]. The ice drift is estimated from the displacement of sea ice for 6 day and 3 day period. The 6 day lag is particularly suitable to capture small displacements which cannot be detected by shorter time lags. The monthly drift data are composed of 5 times the 6 day lag displacement, and if the 6 day lag displacement for a certain grid point is not available, 2 times the 3 day lag displacement is substituted. The product covers nearly the entire Arctic basins except Baffin Bay and the southeastern part of the Greenland Sea. It consists of monthly ice drift from December 1991 until now from September until May. The data are defined on a polar stereographic coordinate system, the horizontal resolution of which is 62.5 km × 62.5 km. We projected the monthly drift from the original coordinate to the comparison grid coordinate with a maximum interpolation distance of 45 km, in the same manner as OSISAF product. It should be noted that the CERSAT monthly product is the only one in our study to be built as a Lagrangian displacement. All the other products in this study are processed into Eulerian averaged monthly displacement vectors.

2.3. KIMURA Product

We also consider ice drift data from Kimura et al. [2013]. Hereafter, we refer to the product as KIMURA. An advantage of this product is that it provides ice drift not only in winter but also in summer, which is appealing to the modeling and data assimilation community [Kimura et al., 2013] (used only the winter data, but summer data are also provided based on the same method). In their work, the ice drift in winter (from December to April) is calculated from brightness temperature maps of AMSR-E 89 GHz horizontal and vertical polarization channels, whereas the ice drift in summer (from May to November) is obtained from those of 18.7 GHz channels. The algorithm used to detect ice motions is the improved MCC method described in Kimura and Wakatsuchi [2000, 2004]. In order to provide ice drift in the entire ice covered area, they filled missing data values by an average of surrounding values, if more than 5 of the surrounding 8 points give an

appropriate ice drift. They repeated this procedure twice for the product. The nominal time interval of consecutive images used to detect ice displacement is 24 h. The data cover the entire Arctic Ocean with a horizontal resolution of $37.5 \text{ km} \times 37.5 \text{ km}$ in winter and with a resolution of $75 \text{ km} \times 75 \text{ km}$ in summer. The data are provided from September 2002 to April 2011. We calculated monthly mean ice drift on the comparison grid coordinate in the same manner as the other products with a maximum interpolation distance of 28 km in winter and 53 km in summer.

2.4. NSIDC Product

NSIDC provides one of the most comprehensive ice drift products for the Arctic Ocean, Polar Pathfinder Daily 25 km EASE-Grid Sea Ice Motion Vectors, Version 2 [Tschudi *et al.*, 2010; Fowler *et al.*, 2013], which currently extends from 1978 to 2012 and covers the entire Arctic Ocean (Hereafter referred to as NSIDC). The product contains daily gridded fields of sea ice motion vectors with estimated error variance (monthly mean gridded product without error variance is also available). The product has been widely used in the modeling and data assimilation community [e.g., Miller *et al.*, 2006; Dai *et al.*, 2006; Stark *et al.*, 2008] and contributed to a number of sea ice studies. The motion algorithm calculates sea ice motions using a variety of satellite-based sensors (Advanced Very High Resolution Radiometer (AVHRR), Scanning Multichannel Microwave Radiometer (SMMR), SSM/I, and AMSR-E), as well as the International Arctic Buoy Program (IABP) observations and wind effects on motion [Thorndike and Colony, 1982]. Note that all passive microwave sensors are used during their time of operation (SMMR until 1987, AMSR-E 2002-2011, SSM/I 1987-present), and that AVHRR use drops after 2006, due to its limited coverage due to cloud cover/contamination. Recent (post-2011) sea ice motions are therefore obtained from SSM/I, IABP buoys, and wind forcing, but the full data set retains the integration of the other sensors during the aforementioned time periods. NCEP Reanalysis wind data were used for the entire data set, provided by the NOAA/OAR/ESRL PSD, Boulder, Colorado, USA, from their Web site at <http://www.esrl.noaa.gov/psd/>. Sea ice motions are obtained from each satellite sensor using the Maximum Cross Correlation (MCC method) and merged with the buoy data and winds using the cokriging estimation method described in Isaaks and Srivastava [1989]. The sea ice motion vectors are defined on Equal Area Scalable Earth Grid (EASE-Grid) with $25 \text{ km} \times 25 \text{ km}$ horizontal resolution on a daily basis. The monthly mean ice drift on the comparison grid is calculated in the same manner as the other products.

Note that we use version 2 of the NSIDC product. We performed the same examinations presented in this paper for the previous version of the NSIDC product (Polar Pathfinder Daily 25 km EASE-Grid Sea Ice Motion Vectors, version 1) [Fowler, 2003], and found that the previous version has a clear bias toward too low speeds in 2006 (not shown). Therefore, we strongly recommend to use the latest version of the NSIDC product for model validation and data assimilation.

2.5. IABP/D Product

In order to get a rough idea regarding the similarity and difference of spatial patterns of ice drift between satellite derived data and buoy measured data, we utilize the interpolated ice velocity field provided from IABP [Thorndike *et al.*, 1983; Colony and Rigor, 1989] (following the naming of the data set, hereafter we refer to the data as IABP/D). The data provide half-daily interpolated ice velocities (x and y components), variance of the interpolation error, and velocity derivatives at grid points on a rectangular coordinate system with a horizontal resolution of roughly 100 km. The objective analysis procedure is based on the optimal interpolation method [Gandin, 1965] and described in Thorndike *et al.* [1983]. We calculated monthly mean ice drift vectors from the half-daily data, and then projected them on the comparison coordinate in the same manner as the satellite derived products. The product provides the variance of the interpolation error as a measure of the distance from the buoy location. As recommended by the data provider, we only use the data whose variance of the interpolation error is less than or equal to 0.5.

2.6. IABP/C Buoy Position Data

For validation purposes of ice-drift products, we also employ ice buoy position data (hereafter referred to as IABP/C) obtained from IABP [Thorndike *et al.*, 1983; Colony and Rigor, 1989]. The data set provides geographical locations of automatic data buoys in the Arctic Ocean from 1979 to 2011 with a half-daily interval. We processed the buoy position data to utilize them for Eulerian-based comparison as follows; First, we calculated half-daily-mean velocity vectors of respective ice buoys on the geographical coordinate from the sequence of buoy positions. Second we defined monthly mean ice drift on the comparison coordinate from an average of half-daily buoy velocities whose initial and terminal locations are contained within a circle

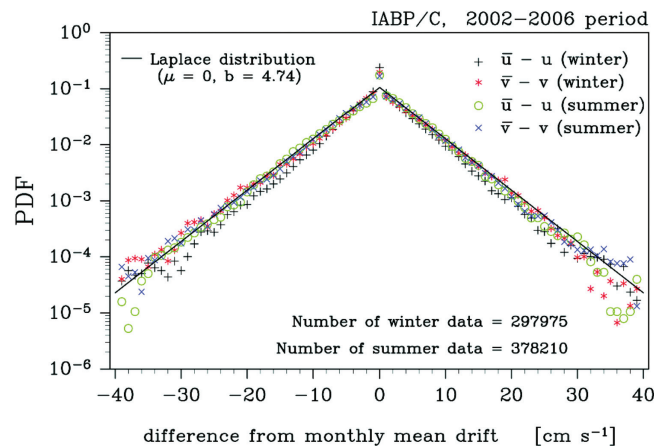


Figure 2. Difference between the monthly mean ice drift at a certain grid point and the half-daily drift used to define the monthly mean. “plus” and “asterisk” denote the difference in x and y direction in winter, while “circle” and “cross” denote those in summer. The black-solid line exhibits a Laplacian distribution, whose standard deviation is calculated from all (winter and summer) data.

point. If not, we defined the drift at the point as a missing value. This criterion corresponds to a temporal coverage of 80% of the respective months.

To estimate the error of the monthly mean data coming from the temporal and spatial interpolation, we examined the distribution of the difference between the monthly mean drift \bar{u} and half-daily drift u_i used to define the monthly mean (Figure 2). In Figure 2, we plotted all combinations of $|\bar{u} - u_i|$ in x and y directions in both seasons. The distribution can be approximated by a Laplacian distribution (black-solid line),

$$f(\bar{u} - u) = \frac{1}{2b} \exp \left[\frac{-|\bar{u} - u_i|}{b} \right], \quad (1)$$

whose variance $2b^2$ is given by

$$b = \sqrt{\frac{1}{2N} \sum_{i=1}^N (u_i - \bar{u})^2}, \quad (2)$$

where N is the number of half-daily drift used to calculate the corresponding monthly mean at a certain grid point. If we estimate the maximum standard error of the monthly mean drift by b/\sqrt{N} , the threshold of 80% temporal coverage gives a standard error of 0.68 cm s^{-1} which we use as an uncertainty of the Eulerian monthly mean drift.

2.7. Ice Concentration

To examine relations between ice concentration and ice drift differences among the products, we use ice concentration data provided from OSISAF. For the data period used in this study (2002–2006), the original data were measured by SSM/I and processed following the algorithms described in *Eastwood et al.* [2010]. Here, we utilize the product named OSI-409, which contains daily mean ice concentration on a polar stereographic grid with a horizontal spacing of 10 km, covering the entire Arctic Ocean. We processed the original OSI-409 data into monthly mean data on the comparison coordinate system to facilitate our comparison. In this process only the original data whose status flag guarantees its reliability were used. Monthly mean values were only defined at a grid point if more than 80% of the days of a months have reliable data. For the data reprojection from the original data grid to the comparison grid, we simply calculated the arithmetical mean of valid data contained in each comparison grid cell. In general, each grid cell contains a sufficient number of data points because of the finer resolution of the ice concentration data, and the interpolation error can be neglected.

2.8. Ice Thickness

A basin-wide ice thickness product provided by *Kwok et al.* [2009] is also used to examine a relationship between ice thickness and ice drift difference among the drift products. The data set is composed of 10

centered at the grid point with a certain radius. We tested several radii for defining the monthly mean drift in order to guarantee robustness of comparison results. We found that choices of radii from 50 to 130 km do not change our qualitative results shown in section 3.4. To calculate the monthly mean drift, we also introduced a criterion for a number of half-daily buoy velocities, which is also essential to guarantee a temporal representativeness of the monthly mean drift. If the number of available data exceeds 48, we defined a monthly mean drift at that

campaigns of Ice, Cloud and land Elevation Satellite (ICESat) from 2003 to 2008 on a polar stereographic grid with a horizontal resolution of 25 km. Ice thickness is estimated by a method described in *Kwok et al.* [2007] and *Kwok and Cunningham* [2008] from total (sea ice plus snow) freeboard measured by a laser altimeter on the satellite. In the present comparison, we utilize seven campaigns (ON03, FM04, ON04, FM05, ON05, FM06, and ON06) during our comparison period. We projected the original data onto the comparison grid by simply adopting the nearest data point, since the horizontal scale of variation of the data is much larger than the resolution of the comparison grid.

3. Analysis of Results

In this section, we first examine similarity and difference of spatial patterns of ice drift from different products and their relation to other sea ice properties. Second, we compare ice-drift speed in various ways (frequencies of occurrence, scatter plots, and time series), and third examine the ice-drift curl which is of relevance for the underlying Arctic Ocean circulation. We fourth make comparisons of the products with buoy drift speeds, and finally we demonstrate uncertainty estimates based on the comparison results. Our comparison focuses mainly on winter (November to April) ice drift which is delivered by all products, while some additional analyses on summer (May to October) ice drift for two products are also provided. For the analyses with respect to time series, we treat October ice drift as winter data in order to extend the temporal window as long as possible.

3.1. Spatial Pattern of Ice Drift

Figure 3 shows an example of the spatial pattern of ice drift of the five products including IABP/D for January 2003. All products show anticyclonic circulation in the Amerasian Basin and cyclonic circulation in the Eurasian Basin. The ice drift speed is intensified along the Alaskan coast, north of Fram Strait and in the northern Barents Sea. The monthly average drift speed in these areas reaches 8 cm s^{-1} in all products. The occurrence of a weak drift area along the Siberian coast and north of the Canadian Archipelago is also common in all products. The spatial pattern of the vectors and their magnitude are consistent with those obtained from buoy observations (Figure 3e).

In contrast to the relatively similar drift patterns shown for January 2003, Figure 4 shows an example for large differences in October 2005. All products show similar spatial pattern of ice drift, such as a broad area of ice-drift vectors pointing towards Svalbard in the central Arctic, an anticyclonic circulation north of Alaska, and a cyclonic circulation north of the Laptev Sea. On the other hand, the magnitude of drift speed and its distribution differ between the products: OSISAF and KIMURA show average drift speeds exceeding 8 cm s^{-1} , extending from the Amerasian Basin to north of Svalbard; CERSAT shows its maximum drift speed mostly in the Amerasian Basin and slower speed in the Eurasian Basin; compared to the other products NSIDC shows slower drift speed in the central Arctic. In the south of Fram Strait, KIMURA and NSIDC exhibit strong southward drift vectors, which are not evident in CERSAT. The common features found in the Amerasian Basin are consistent with the interpolated buoy ice drift of IABP/D, while the differences found in the Eurasian Basin and south of Fram Strait cannot be compared with IABP/D due to the lack of buoy data (Figure 4f). It is also interesting to note the spatial scale of drift speed variations. CERSAT exhibits small-scale variation in the Eurasian Basin side, which are not evident in the other products.

Rampal et al. [2009] analyzed buoy trajectories in the Arctic Ocean as the superposition of a mean field and fluctuations, and estimated appropriate spatial and temporal scales for separation between the mean and fluctuations as 400 km and 160 days for winter. Here we adopt these scales to divide the ice motion into a mean field and fluctuations. The mean ice motion in winter is defined as

$$\bar{\mathbf{u}}^W = \frac{1}{J} \sum_{j=1}^J \int_{L=400\text{km}} \mathbf{G} [\mathbf{u}], \quad (3)$$

where \mathbf{u} is the monthly mean ice drift vector at a certain point, $\mathbf{G}_{L=400\text{km}}$ is a Gaussian filter with 400 km spatial scale, and J is the number of monthly mean data used to define the mean field ($J = 5$). We used monthly mean data from December to April to define the temporal average of the ice drift. Figure 5 shows spatial patterns of mean ice drift difference among the products averaged over the four winter seasons. For example, the mean difference of ice drift at a given grid point between OSISAF and CERSAT is given by

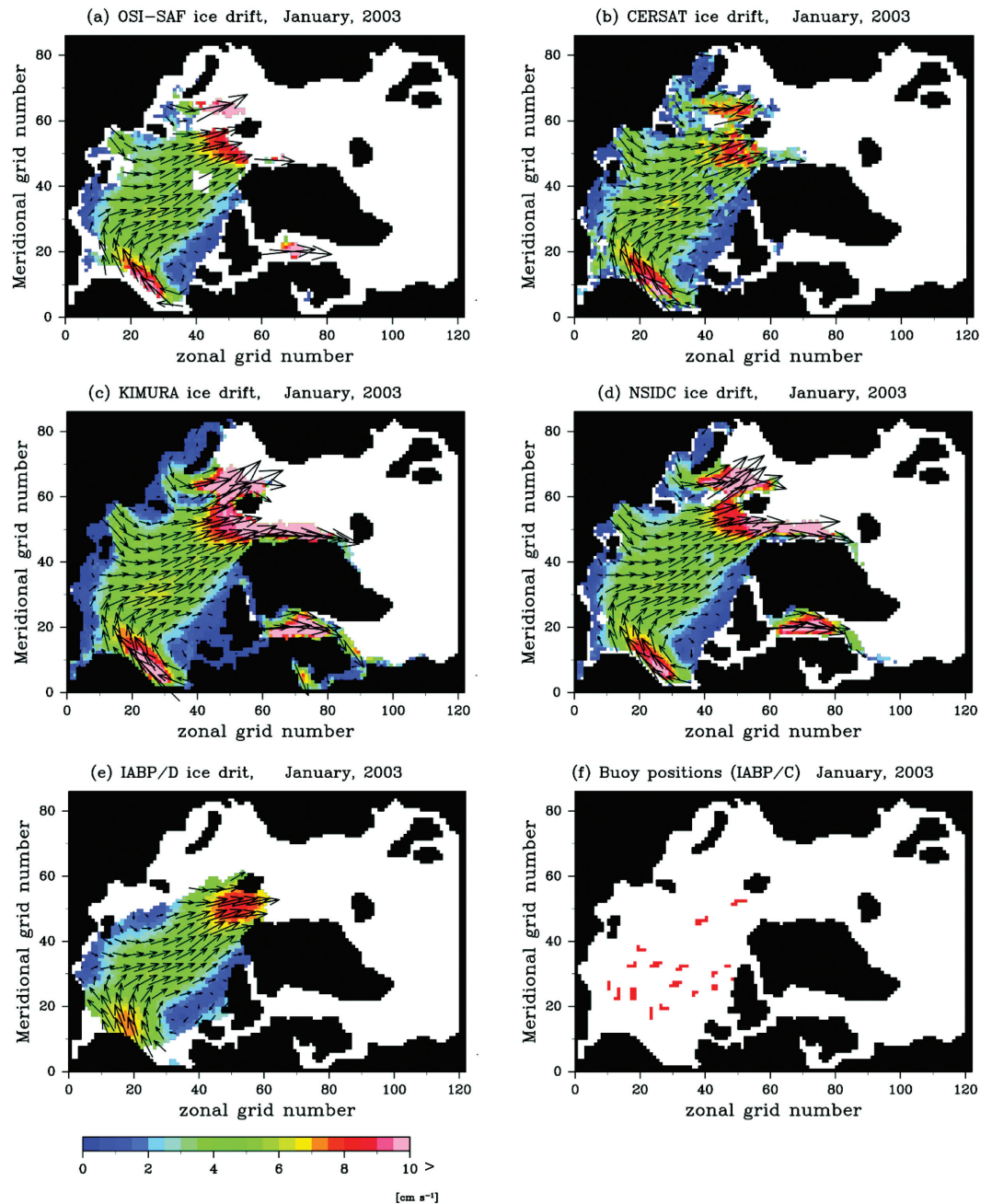


Figure 3. Monthly mean ice drift vectors from (a) OSISAF, (b) CERSAT, (c) KIMURA, (d) NSIDC, and (e) IABP/D in January 2003 and (f) the locations of ice buoys in this time period. For IABP/D drift in Figure 3e only the grid points where the variance of interpolation error is less than or equal to 0.5 were used. The color bar showing ice drift speed in Figure 3e is used for all plots.

$|\overline{\mathbf{U}}_{diff}^W| = |\overline{\mathbf{U}}_{OSISAF}^W - \overline{\mathbf{U}}_{CERSAT}^W|$, where $|\mathbf{A}|$ is the average of the absolute value of a vector \mathbf{A} over the four winter seasons. The figure clearly shows that the differences of the drift vectors are not spatially uniform. In the central Arctic, the differences are relatively small ($< 0.4 \text{ cm s}^{-1}$), whereas the differences are large ($0.5\text{--}2.0 \text{ cm s}^{-1}$) in the peripheral ice-covered areas such as north of the Alaskan coast and in the Barents Sea, the Kara Sea, and the Greenland Sea. Although the magnitude of the difference depends on the combination of the products, the spatial patterns of the differences are similar for all combinations of the products. The difference of the fluctuation fields, such as $|\overline{\mathbf{U}}'_{diff}| = |\overline{\mathbf{U}}'_{OSISAF} - \overline{\mathbf{U}}'_{CERSAT}|$, where the respective fluctuations are given by $\mathbf{U}'_{OSISAF} = \mathbf{U}_{OSISAF} - \overline{\mathbf{U}}_{OSISAF}^W$ and $\mathbf{U}'_{CERSAT} = \mathbf{U}_{CERSAT} - \overline{\mathbf{U}}_{CERSAT}^W$, also exhibits similar spatial patterns (not shown).

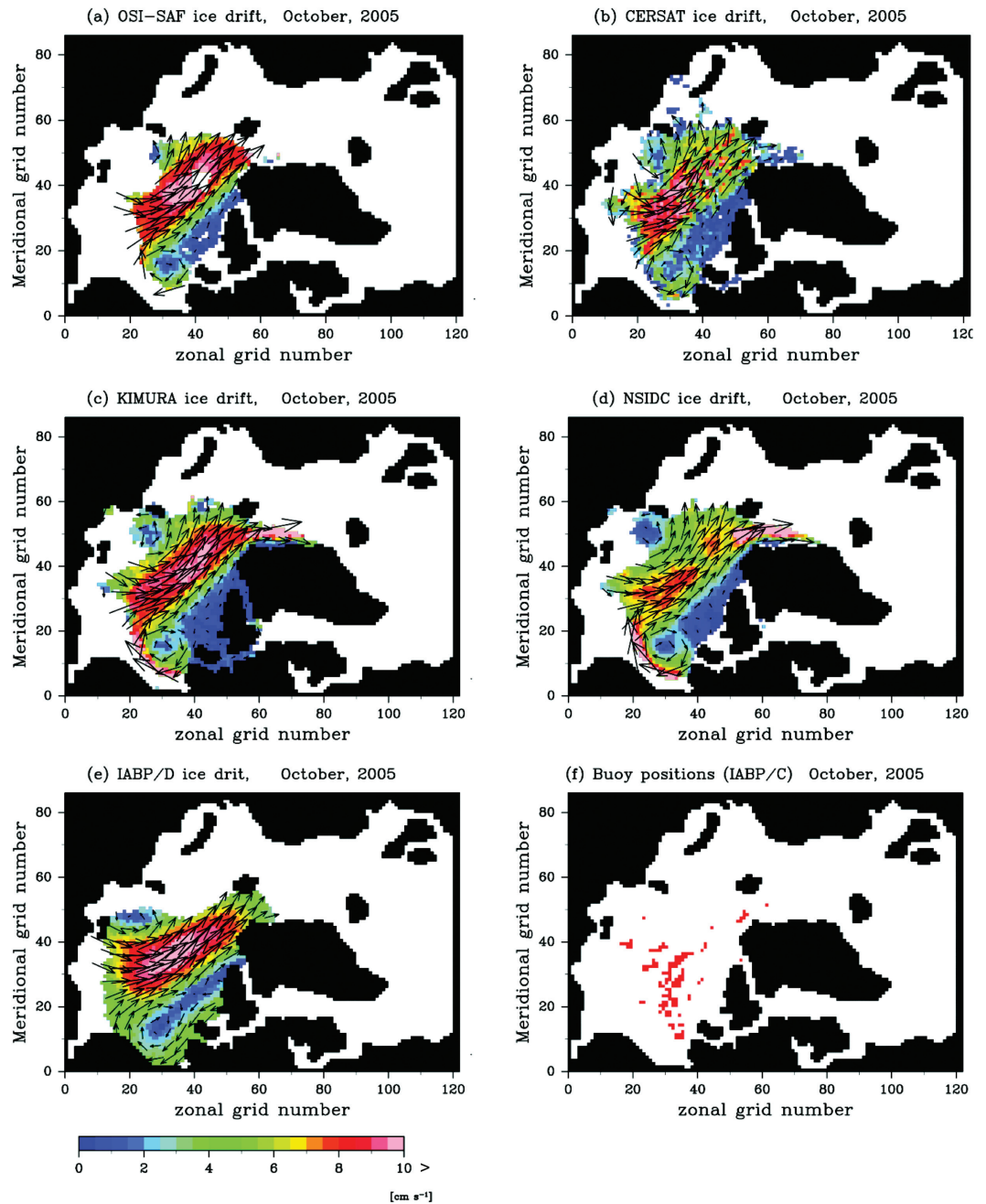


Figure 4. The same as Figure 2, but for January 2006.

The areas showing large differences are those of peripheral basins, with relatively small ice concentration. Figure 6a shows mean ice concentration averaged over the winter seasons from 2002 to 2006. In the areas of small ice drift differences, mean ice concentration (Figure 6a) is almost everywhere larger than 97%, whereas in areas of large differences, ice concentration ranges from roughly 90–97%. The relation between ice drift difference and ice concentration is revealed in a scatter plot (Figure 7). It shows the difference of monthly mean ice drift (magnitude of the difference vector) between two products as a function of ice concentration. Each light-blue point corresponds to a difference of monthly mean drift at a certain grid point and at a certain month, while each red cross denotes the mean difference at a certain ice concentration bin. The difference is small ($0.6\text{--}0.8\text{ cm s}^{-1}$) in 99–100% ice concentration area, and gradually increases to $0.9\text{--}4.4\text{ cm s}^{-1}$ in 89–90% concentration area. The mean difference of drift in the 89–90% ice concentration

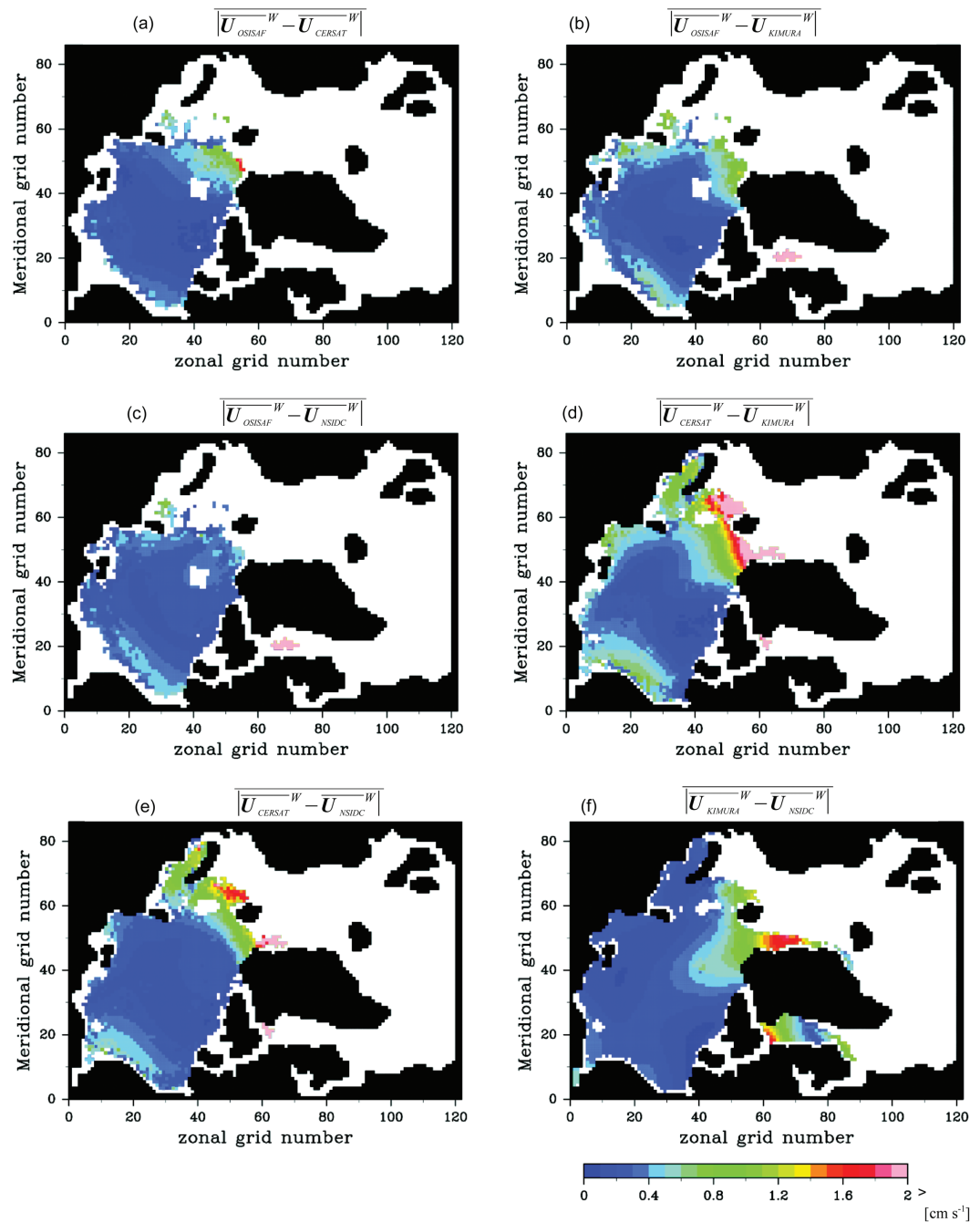


Figure 5. Difference of monthly mean ice drift between (a) OSISAF and CERSAT, (b) OSISAF and KIMURA, (c) OSISAF and NSIDC, (d) CERSAT and KIMURA, (e) CERSAT and NSIDC, and (f) KIMURA and NSIDC averaged over the four winter seasons.

area is 2–5 times larger than that in the 99–100% concentration area, depending on the choice of ice drift products.

We also examined the relation between ice-drift differences and ice thicknesses. Although the spatial pattern of ice thickness is not necessarily similar to that of small drift differences, a large part of the area of thick ice (> 3 m) is contained in the high ice concentration area (Figure 6b). To plot the ice drift difference as a function of ice thickness, we used ice thickness data obtained from ICESat campaigns from 2003 to 2006. Since the product provides averaged ice thicknesses for time periods of 34–55 days which do not coincide with calendar month, we choose the calendar months with the largest number of matching days

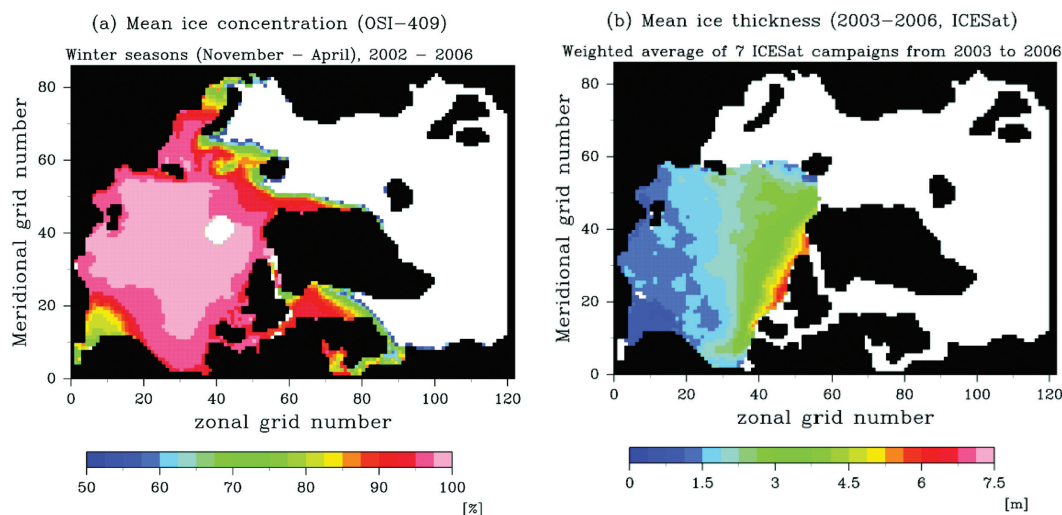


Figure 6. Mean ice concentration averaged over the winter seasons of the comparison period (a) and mean ice thickness of 7 ICESat campaigns from 2003 to 2006 (b). The mean ice concentration is calculated from OSI-409 daily sea-ice concentrations. The mean ice thickness is calculated from weighted average of ON03, FM04, ON04, FM05, ON05, FM06, and ON06 campaigns of ICESat.

for the analysis. This procedure introduces a certain amount of uncertainty but since the ice thicknesses are not very quickly changing in time, we expect only a moderate effect which is certainly lower than the estimated uncertainty of the ICESat product of about 50 cm [Kwok *et al.*, 2009; see Zygmuntowska *et al.* [2013] for a recent discussion on the uncertainties). Accordingly, Figure 8 shows the ice-drift differences as a function of ice thicknesses. A light-blue dot corresponds to a difference of monthly mean drift at a certain grid point and at a certain month, whereas a red-cross denotes the average of the ice drift within a 50 cm ice thickness bin. Except for the combinations including OSISAF, we find a clear tendency to small (large) differences at large (small) ice thicknesses (see Appendix A for statistical tests on the significance of the difference). The mean differences of ice drift in the 1.0–1.5 m thickness range from 0.7 to 1.9 cm s^{-1} whereas those in the 4.5–5 m thickness range are 0.5–0.8 cm s^{-1} .

The relations we found between monthly difference in drift speed and monthly ice concentration or thickness are probably not holding for the corresponding daily fields, and we do not infer that daily ice concentration or thickness can be used as proxies for uncertainties of daily ice motion vectors. The correlation to ice concentration on monthly timescale is indeed probably related to the fact that regions with relatively low ice concentration are regions where ice froze or retreated during the course of the month (Figure 6a). It is well known by ice motion data producers that ice motion is more uncertain during the freezing and early melting periods due to enhanced atmospheric influence on the satellite signal, and more rapid changes of sea-ice surface emissivity and backscatter. In addition, ice motion vectors retrieved in the vicinity of the ice edge, or more generally at times when sea ice does not completely fill the central Arctic Ocean are more uncertain, since the motion field is less spatially coherent than far in the ice pack, or when sea ice motion is constrained by land boundaries [Lavergne *et al.*, 2010]. As far as ice thickness is concerned, it is strongly linked in the Arctic Ocean to the age of the ice, which itself is correlated to surface emissivity characteristics that have a strong influence on the accuracy of the ice motion algorithms. Although monthly ice concentration and thickness prove to be useful proxies for parameterizing ice motion uncertainty on a monthly scale, it is probably via complex error propagation mechanisms and correlations with other factors, therefore our results should not be applied to shorter timescales.

3.2. Ice Drift Speed

Figure 9 shows the frequency distribution of mean and fluctuation ice drift speed in winter obtained from the four products. The definition of the mean and fluctuation is given in section 3.1. Only data points common to all products are used (i.e., if one or more of the products have a missing value at a certain point, the data at that point are not taken into account). For winter mean velocity, all products show similar frequency with the bulk occurrences in the range of 1–3 cm s^{-1} , whereas the shape of the tails toward the larger velocities differs between the products; CERSAT exhibits the shortest tail with the maximum speed of less

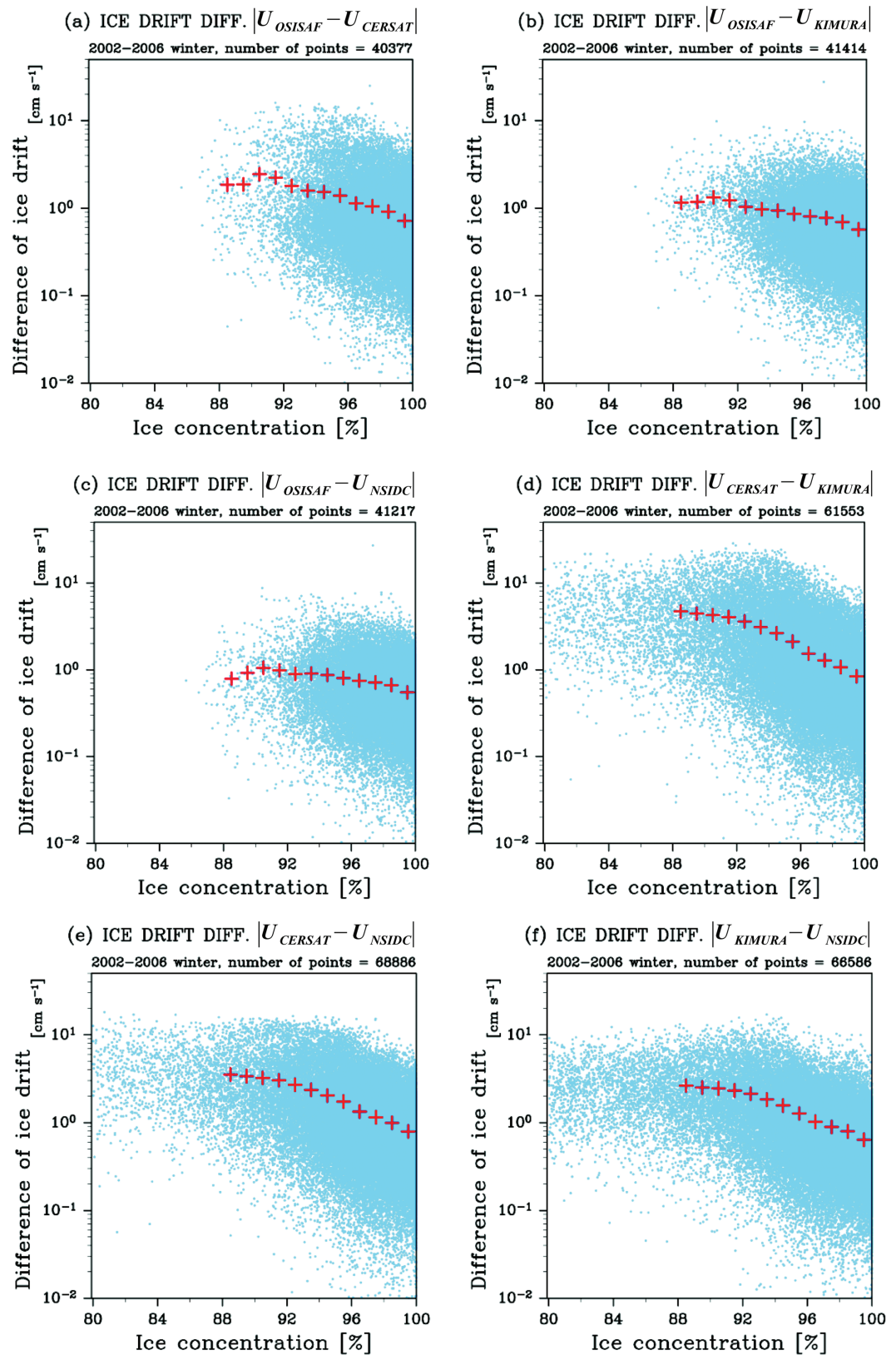


Figure 7. Difference of monthly mean ice drift between (a) OSISAF and CERSAT, (b) OSISAF and KIMURA, (c) OSISAF and NSIDC, (d) CERSAT and KIMURA, (e) CERSAT and NSIDC and (f) KIMURA and NSIDC as a function of the ice concentration. The light-blue dots correspond to the mean drift differences in winter at every grid point and the red crosses denote the mean difference in a certain ice-concentration bin.

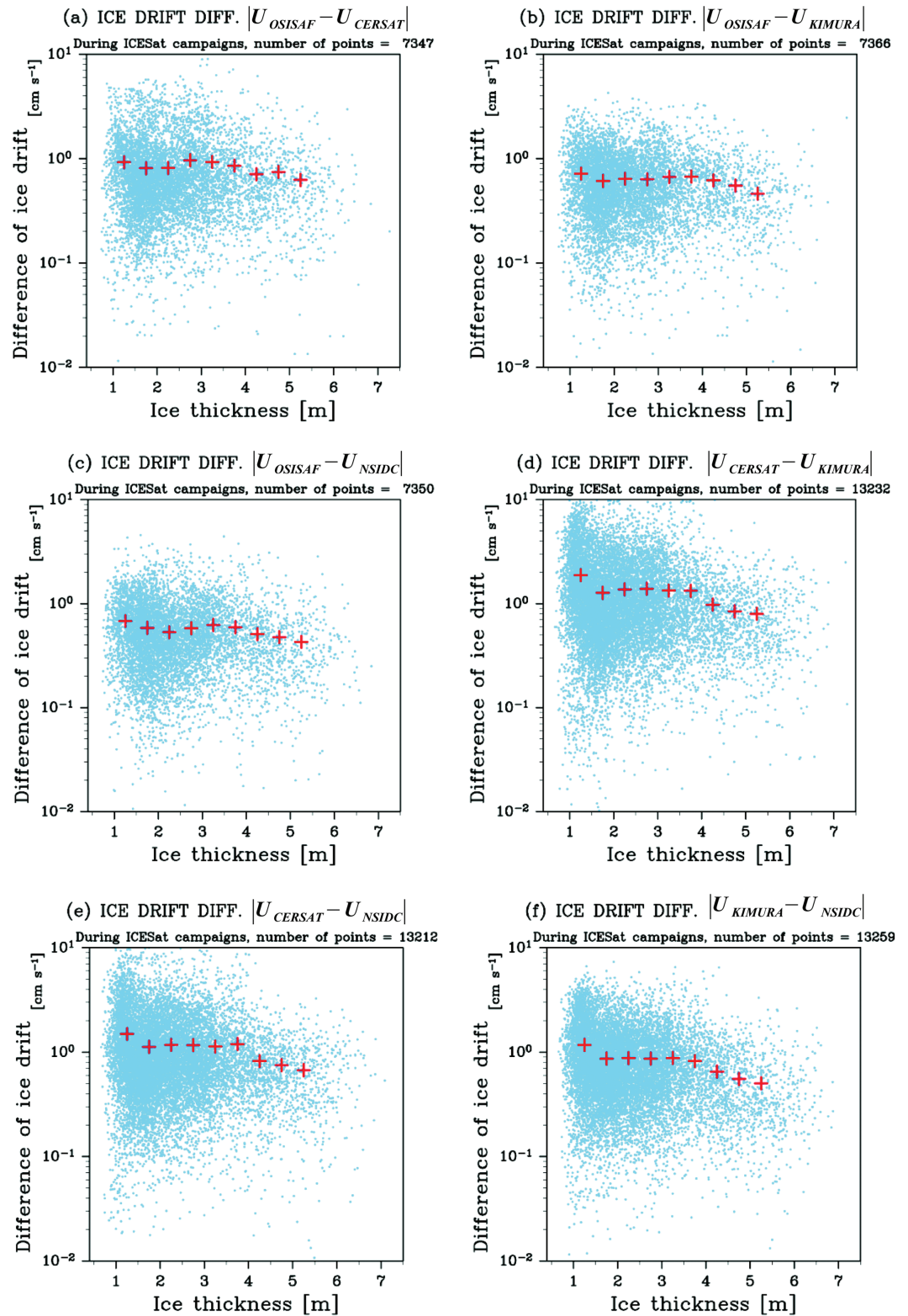


Figure 8. Difference of monthly mean ice drift speed at respective grid points between (a) OSISAF and CERSAT, (b) OSISAF and KIMURA, (c) OSISAF and NSIDC, (d) CERSAT and KIMURA, (e) CERSAT and NSIDC, and (f) KIMURA and NSIDC as a function of ice thickness. The light-blue dots correspond to the mean drift differences in winter at every grid point and the red crosses denote the mean difference in a certain ice-thickness bin.

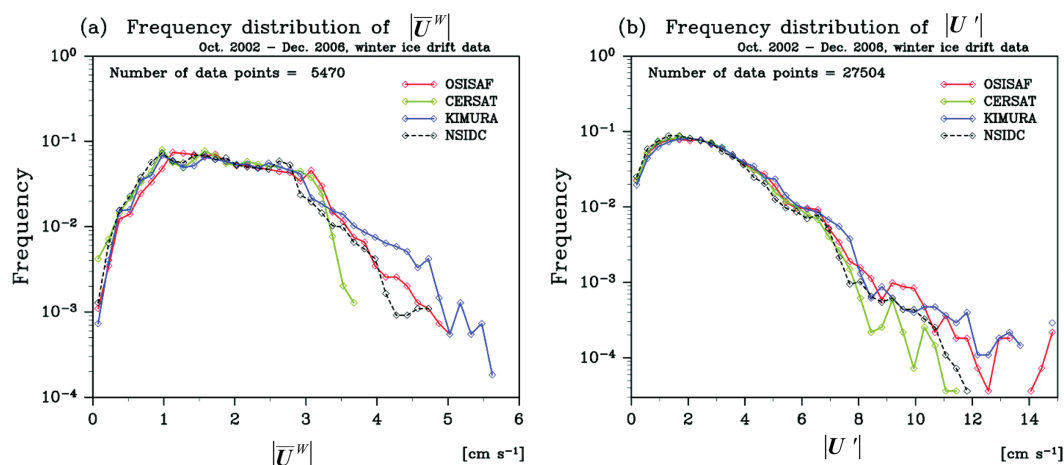


Figure 9. Frequency distribution of (a) winter mean ice drift velocity and (b) winter fluctuation velocity. Red, green, blue, and black diamonds denote OSISAF, CERSAT, KIMURA, and NSIDC, respectively.

than 4 cm s^{-1} , OSISAF and NSIDC exhibit similar and moderate tails up to 5 cm s^{-1} , and KIMURA exhibits the longest tail exceeding 5 cm s^{-1} . For the fluctuation part of the velocity (Figure 9b), all products show similar distribution of frequencies from 0 to about 5 cm s^{-1} , and shows slightly different shape of the tails for drift speeds higher than 7 cm s^{-1} . However, the spread of the tails is smaller than those found in the frequency distribution of the winter mean velocities. The average of winter mean drift speeds range from 1.8 cm s^{-1} (CERSAT and NSIDC) to 2.0 cm s^{-1} (KIMURA), and those of winter fluctuation range from 2.5 cm s^{-1} (NSIDC) to 2.8 cm s^{-1} (KIMURA), i.e., the differences are lower than about 10%.

Scatter plots of drift speeds from all combinations of the products are shown in Figure 10. We plotted the natural logarithm of density of points obtained from respective monthly mean drift velocities in the winter season (November to April) from 2002 to 2006. The highest correlation is found in the combinations between OSISAF and NSIDC and between OSISAF and KIMURA (Figure 10b and 10c, $r = 0.96$) while the lowest correlation is found between CERSAT and KIMURA (Figure 10d, $r = 0.62$). The root mean square differences (RMSDs) between the products ranges from 0.73 cm s^{-1} (OSISAF versus NSIDC) to 2.64 cm s^{-1} (CERSAT versus KIMURA). The stripe feature of CERSAT drift speed in Figure 10a, 10d, and 10e are due to the quantization noise inherent to the MCC method. The quantization noise effectively acts as a rounding operator, and is also the reason why CERSAT is the only product in our study exhibiting velocities that are exactly zero.

A time series of Arctic-wide mean ice drift is plotted in Figure 11. Only the grid points containing ice drift for all four products (in summer only KIMURA and NSIDC) and the IABP/D ice drift are used to calculate the spatial mean (OSISAF is excluded from the time series in October and November 2003, since we cannot calculate monthly mean drift for this 2 months by using the 90% threshold). It should be noted that the time series is a valid measure for the difference between the products at each month, whereas it should not be regarded as an unbiased estimate of temporal variation of the quantities, since the sample area varies from month to month and year to year (this also holds for the time series shown later Figures 12, 16, and 17). In winter, all products show similar temporal variation, while the magnitude of the positive peaks differs by more than 1 cm s^{-1} at maximum. By and large CERSAT exhibits slightly slower drift speed compared to the others, consistent with the frequency of occurrence shown in Figure 9. The temporal variations of the four products are also similar to that of IABP/D. The correlations between the respective products and the IABP/D are larger than 0.9; however, explained variances vary from 0.68 for OSISAF, 0.56 for KIMURA, 0.82 for CERSAT to 0.84 for NSIDC reflecting the occurrences of large ice drift speeds in OSISAF and KIMURA not obtained by IABP/D and probably the use of buoy data in the NSIDC product. In summer, on the other hand, KIMURA and NSIDC are only partly covariant (pink-shaded periods in Figure 11). KIMURA exhibits faster drift speed compared to NSIDC of 0.93 cm s^{-1} on average. Correlation coefficients with IABP/D are 0.90 (KIMURA) and 0.85 (NSIDC), respectively, but KIMURA explains much more variance than NSIDC (0.75 and 0.30, respectively).

Such a seasonal dependence of the differences can be also found in a known characteristic feature of Arctic sea ice motion, namely the Transpolar Drift (TPD). Figure 12 shows the temporal variation of the TPD from

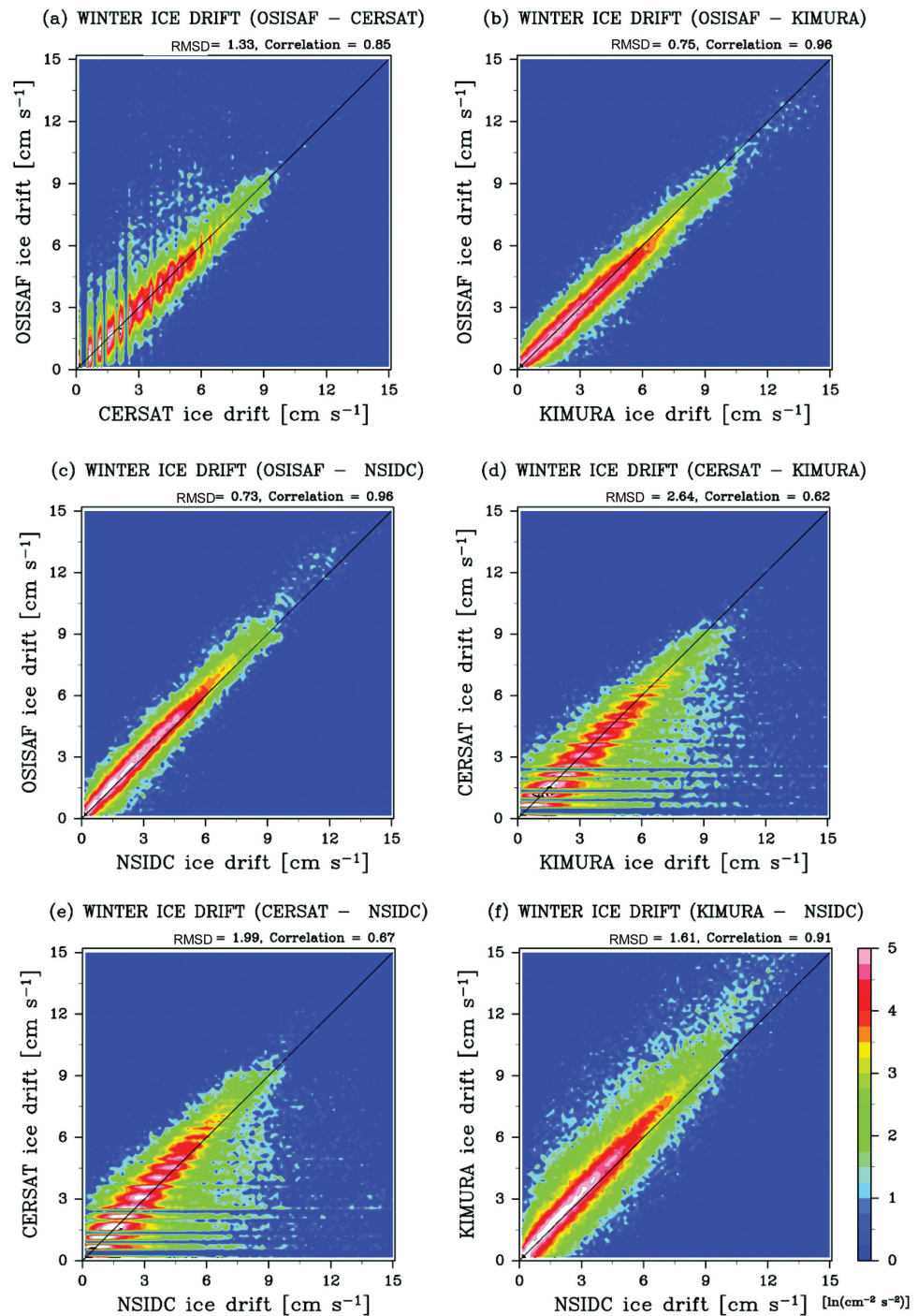


Figure 10. Scatter plot of monthly mean ice drift speed in winter between (a) OSISAF and CERSAT, (b) OSISAF and KIMURA, (c) OSISAF and NSIDC, (d) CERSAT and KIMURA, (e) CERSAT and NSIDC, and (f) KIMURA and NSIDC. The color shows the natural logarithm of the density of points (cm⁻² s⁻²).

September 2002 to December 2006 for all products. The TPD is calculated as the spatial average of all ice drift vectors located in the shaded area in Figure 12a pointing in the direction of the arrow also shown in the plot. Only grid points for which all the products provide valid values were used. In winter, all products vary coherently with comparable TPD speed (the mean difference between the four products is 0.32 cm s⁻¹) and is consistent with the IABP/D drift (the mean difference is 0.36 cm s⁻¹). In summer, the temporal variations of KIMURA and NSIDC are less coherent (the mean difference is 0.72 cm s⁻¹) and the differences from the IABP/D are also large (0.79 cm s⁻¹ on average). It is worth noting that even with similar drift

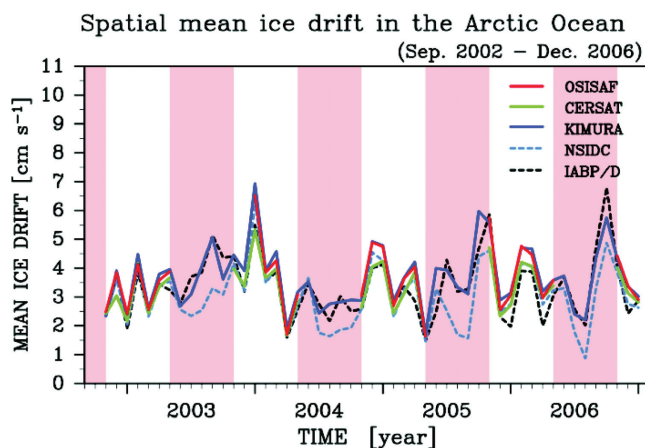


Figure 11. Time series of the spatial mean ice drift speed in the Arctic Ocean. Only grid cells for which all the products provide valid values are used to calculate the spatial mean. From October to April, grid cells common to OSISAF, CERSAT, KIMURA, NSIDC, and IABP/D are used to calculate the mean, whereas from May to September (shaded periods) grid cells common to KIMURA, NSIDC, and IABP/D are used. For October and November of 2003, OSISAF is excluded from the time series, since we cannot define monthly mean value due to too many daily data gaps.

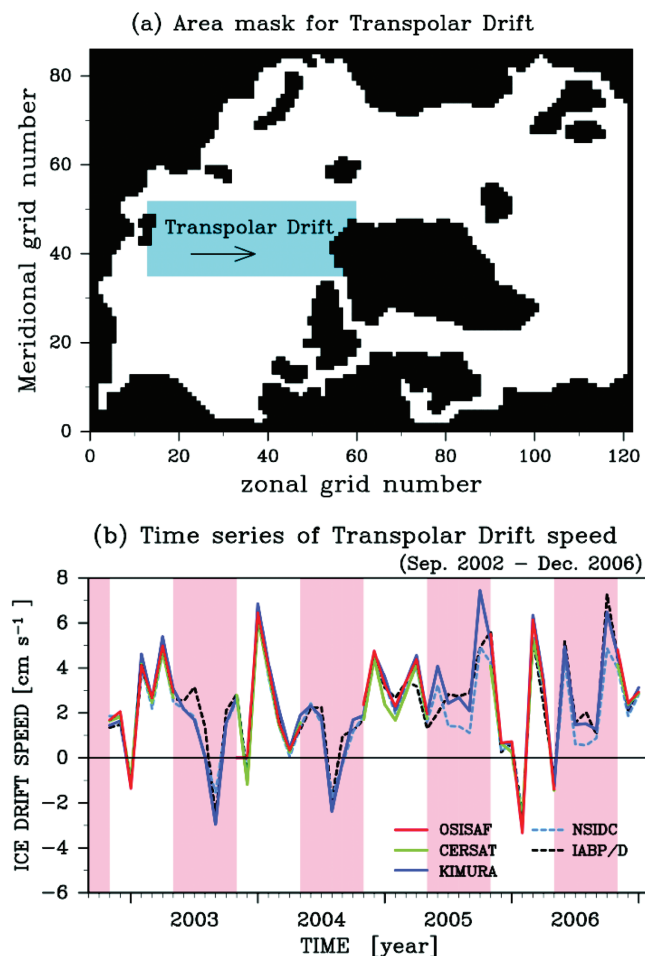


Figure 12. Area mask (a) and time series (b) of the transpolar drift speed. The transpolar drift speed is calculated by the spatial mean of vector component pointing in the direction of the arrow shown in Figure 12a. Only grid points in which all products give valid data are used to calculate the mean.

speeds in winter, the mean difference among the products (0.32 cm s^{-1}) comes up to 13% of the mean TPD speed (2.39 cm s^{-1}). For summer, the difference between KIMURA and NSIDC (0.72 cm s^{-1}) reaches 41% of the mean TPD speed (1.76 cm s^{-1}).

3.3. Ice Drift Curl

Ice drift curl is one of the drivers of the ocean circulation under the ice through vorticity input. Figure 13 shows the spatial patterns of the ice drift curl in January 2003 (see the mean ice drift in Figure 3). All products show similar curl on a basin-wide scale; negative ice drift curl in the Amerasian Basin and positive curl in the Eurasian Basin. These basin-wide scale patterns are qualitatively consistent with those calculated from the IABP/D drift (Figure 13e). The magnitude of the curl is comparable among the products, although the extreme are larger than those observed in IABP/D. All products show small-scale structures not contained in the IABP/D data. This reinforces that the satellite-derived drift has a suitable resolution for a validation of medium resolution sea ice models and is favorable to capture sharper spatial gradients of ice drift. Although based on local-scale buoy velocity data, IABP/D is a spatially interpolated field that probably smooths most of the deformations and gradients of the ice drift including the basin-scale curl.

Figure 14 shows another example of spatial patterns of ice-drift curl corresponding to the ice drift shown in Figure 4. Although the basin-scale spatial patterns are similar among the products, the small-scale extensions of positive and negative curls and spatial scale of

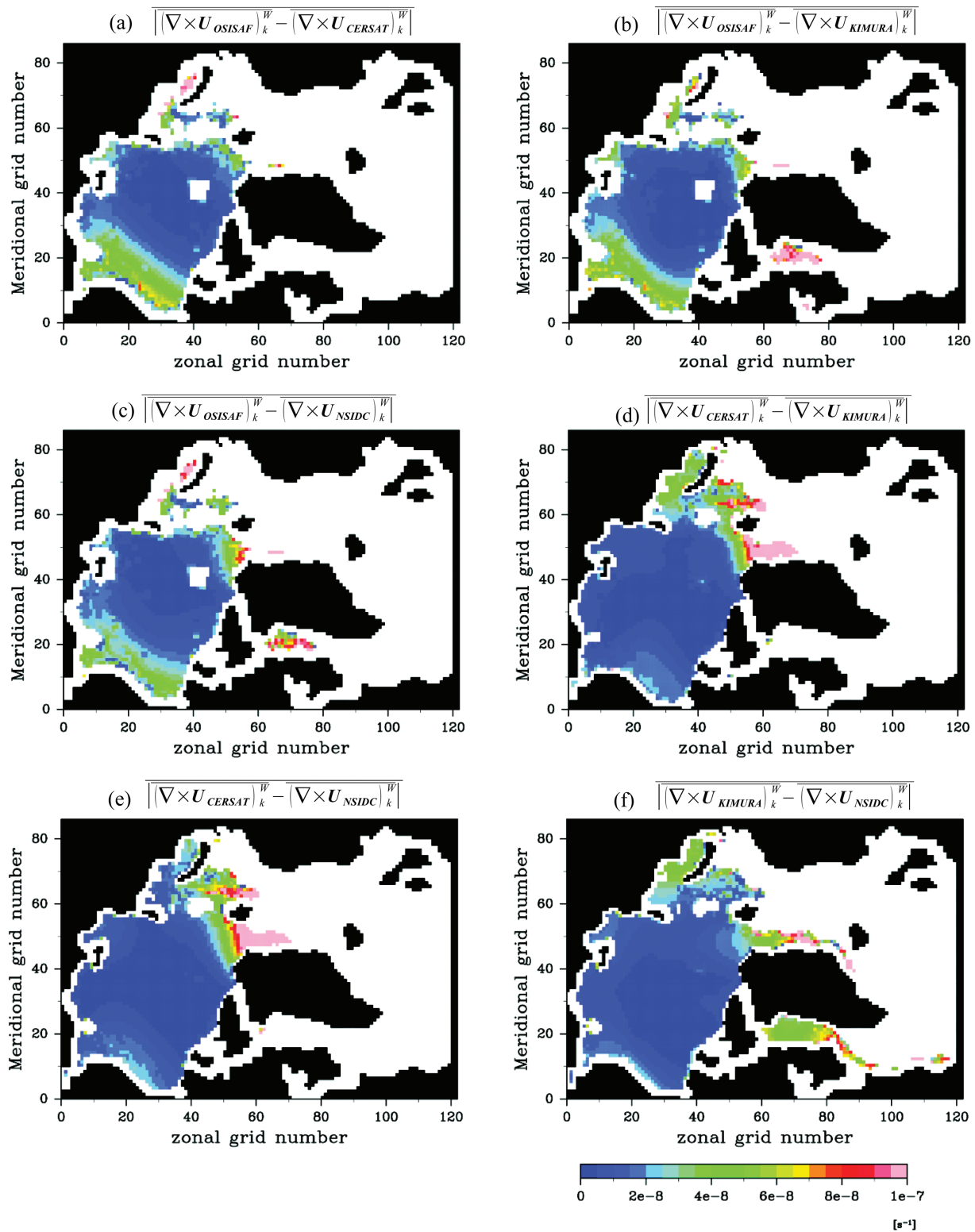


Figure 15. Difference of mean ice drift curl in winter between (a) OSISAF and CERSAT, (b) OSISAF and KIMURA, (c) OSISAF and NSIDC, (d) CERSAT and KIMURA, (e) CERSAT and NSIDC, and (f) KIMURA and NSIDC averaged over the four winter seasons. See the main text for a detailed description.

as suggested by Rampal et al. [2009]. The differences are not spatially uniform, but are emphasized in some specific regions. Similar to the differences of the mean ice drift speed (Figure 5), the differences are relatively large in the southern part of the Canadian Basin and in the marginal seas on the Eurasian side of the Arctic Ocean.

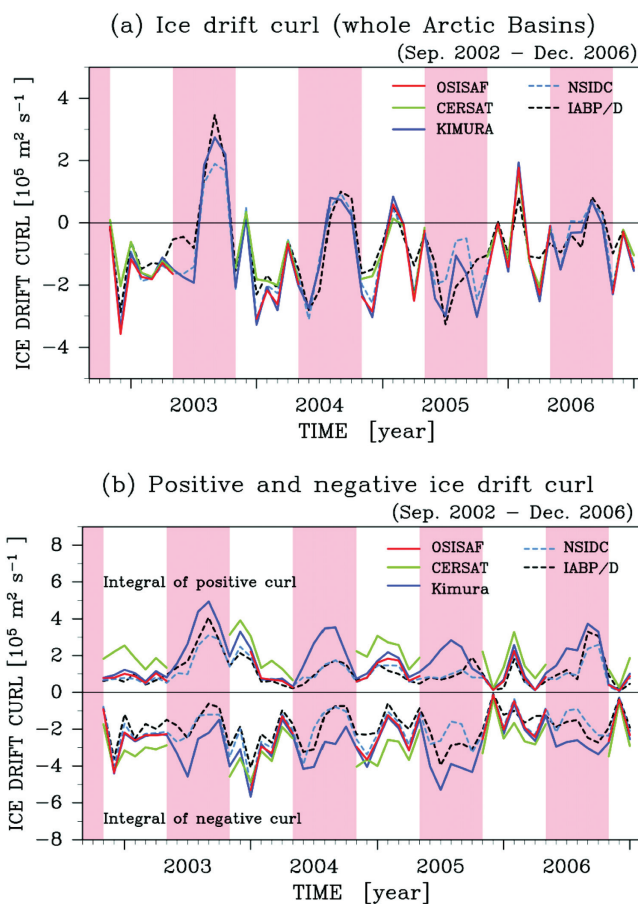


Figure 16. Time series of monthly mean ice drift curl (a) integrated in the whole Arctic basins and (b) integrated over positive and negative areas separately. Only the grid points in which all the products (including IABP/D data whose variance of interpolation error is less than or equal to 0.5) provide valid ice drift were used to calculate ice drift curl, i.e., in winter (October to April) grid cells valid in all products were used (except for October and November of 2003), while in summer (May to September) those with valid ice drift in KIMURA, NSIDC, and IABP/D were used for the calculation. For October and November 2003, OSISAF data are excluded, because we cannot define monthly mean drift due to daily data gaps.

the products in winter is $2.3 \times 10^4 \text{ m}^2 \text{ s}^{-1}$ on average, which is 18% of the mean ice drift curl. The mean differences between the products and IABP/D in winter are 39–54% of the temporal average of IABP/D ice drift curl ($-9.8 \times 10^4 \text{ m}^2 \text{ s}^{-1}$). If we separate the integral of the curl in positive and negative areas (Figure 16b), OSISAF and KIMURA show quite similar temporal variations. CERSAT generally exhibits larger magnitude of positive and negative values compared to the other products, presumably associated with its small-scale fluctuations (see also Figures 13b and 14b). NSIDC generally exhibits slightly smaller magnitude of positive and negative curls compared to the other three products, whereas it is closest to the IABP/D curl.

Regarding ice drift curl in summer, the difference between KIMURA and NSIDC is large compared to that in winter (mean difference in winter $1.8 \times 10^4 \text{ m}^2 \text{ s}^{-1}$ and in summer $4.3 \times 10^4 \text{ m}^2 \text{ s}^{-1}$). The mean difference between the products and IABP/D in summer is comparable to the magnitude of the temporal average of the IABP/D ice drift curl. KIMURA generally gives larger magnitude of positive and negative curls compared to IABP/D, whereas NSIDC generally gives smaller magnitude of curls compared to IABP/D (Figure 16b).

Sea ice motion in the Arctic Ocean is characterized by a strong anticyclonic circulation in the Amerasian Basin and a cyclonic circulation in the Eurasian Basin divided by the Transpolar drift [e.g., *Colony and Thorndike, 1984; Emery et al., 1997*]. The strength of these features are oscillating with a period of several years [Proshutinsky and Johnson, 1997; Proshutinsky et al., 2009], and provide a distinctive feature of basin-scale sea-ice motion. We divided the Amerasian and Eurasian Basins by the area mask shown in Figure 17a and calculated the spatial

To quantitatively compare the products, we plotted the time series of ice drift curl in Figure 16. It shows the spatially integrated ice drift curl in the Arctic Ocean. Again, only grid points in which all products provide valid values were used (except for October and November 2003). Figure 16a depicts the integral in the whole basins in the Arctic, and Figure 16b separately depicts the integral in positive and negative areas. It should be noted again that these time series are a valid measure for the intercomparison of the products, but cannot be seen as an unbiased measure of the ice drift curl in the Arctic Ocean since we used only grid points where data for all products and IABP/D drift exist.

All products vary coherently in winter, whereas the magnitude of the positive and negative peaks sometimes agrees well and sometimes disagrees considerably. Particularly, differences of negative peaks (e.g., November 2002, December 2003, November 2004) are much larger than those of positive peaks (e.g., November 2003, January 2005, January 2006). The difference among

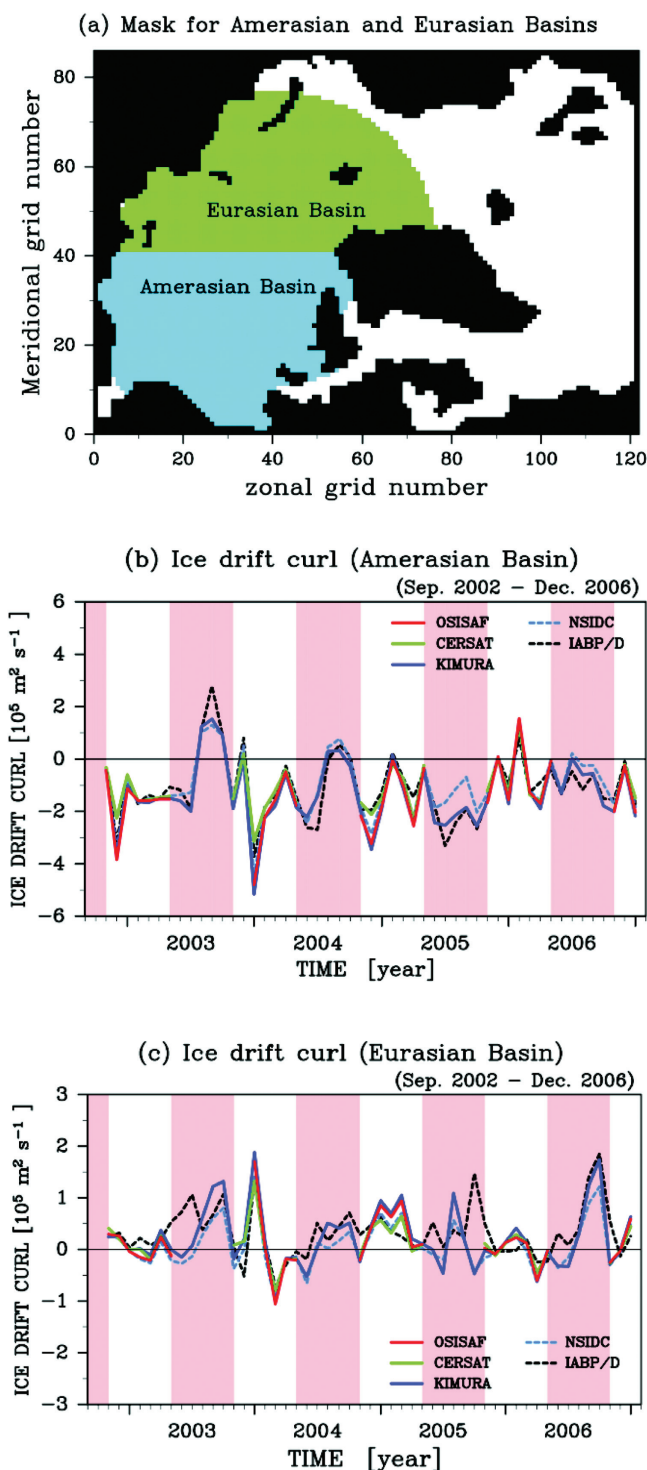


Figure 17. Area mask (a) and time series of ice drift curl in the (b) Amerasian and the (c) Eurasian Basins. Only the grid points in which all the products (including IABP/D) provide valid data were used to calculate spatial integral of the curl.

integral of ice-drift curl in these areas (Figure 17b and 17c). In the Amerasian Basin, all products exhibit similar temporal variation in winter, whereas the magnitude of the negative peaks (e.g., November 2002, December 2003, November 2004) differs significantly. The differences of the peaks among the products are comparable to the peak values (Figure 17b), which leads to a maximal difference of mean ice-drift curl in winter of 24% ($3.3 \times 10^4 \text{ m}^2 \text{ s}^{-1}$) (The ratio is calculated by the maximum difference divided by the average of the four products). In summer, KIMURA and NSIDC exhibit less coherent variations than in winter. The difference between the products comes up to 37% of the mean ice-drift curl in summer.

In the Eurasian Basin, the time series of ice-drift curl show more diverging features (Figure 17c) probably related to the lower ice concentrations (see also Figure 7). The temporal variations in winter are similar to some extent, whereas the magnitude of peaks sometimes differs significantly. In summer, it is difficult to find a correspondence between KIMURA and NSIDC and also with IABP/D.

3.4. Comparison With Buoy Drift Data

To examine the uncertainty of the monthly mean ice drift, we compare the drift products with the one obtained from in situ buoy observations. The validations of the original products can be found in papers cited in section 2, while the error estimate for the original data cannot be directly applied

to the monthly mean values except to CERSAT, since temporal error covariance is generally not available. As a counterpart to satellite derived data, we calculated monthly mean ice drift from the buoy positions (IABP/C) at the grid points where the buoy data are available (see section 2.6 for the description). This data processing allows for a comparison of the drift on the same location and at the same time. Comparisons of

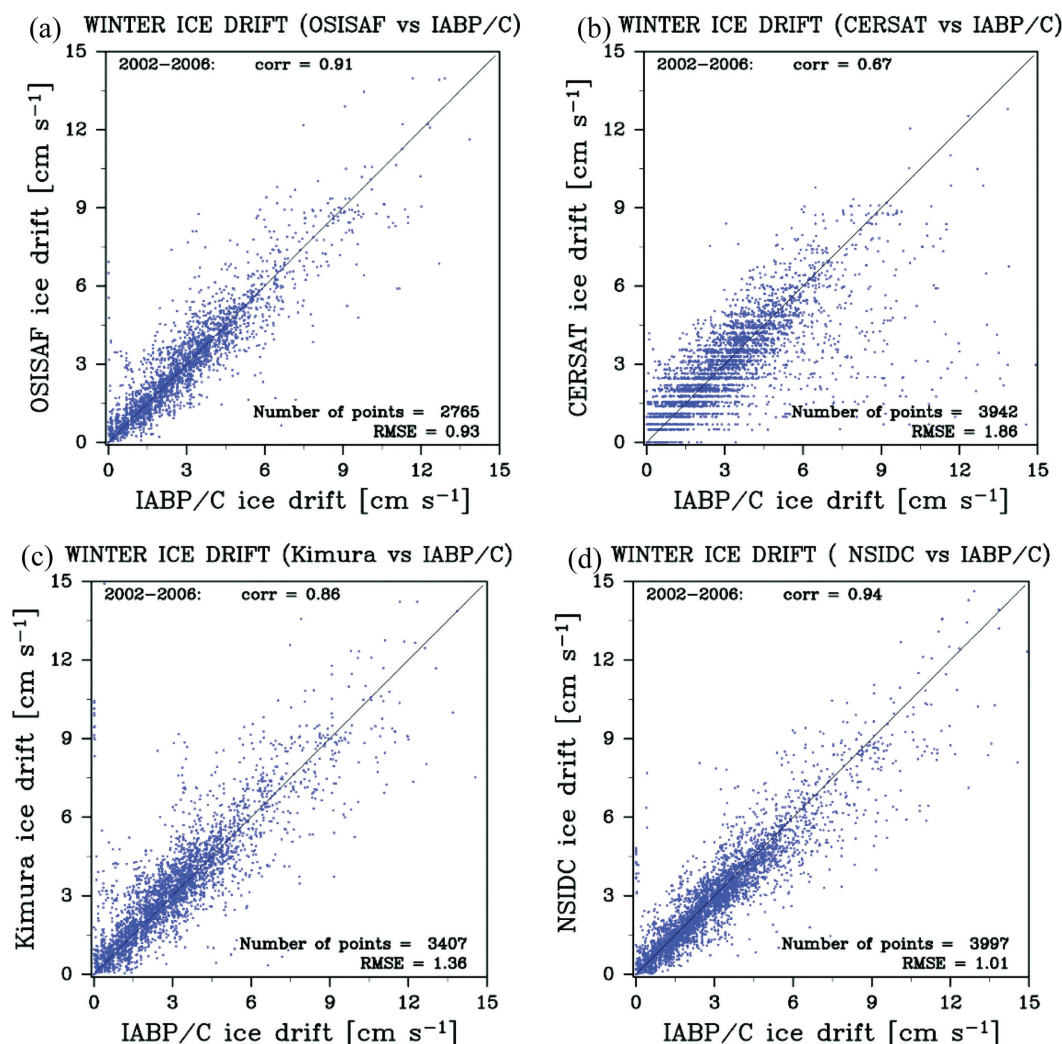


Figure 18. Scatter plot of monthly mean ice drift speed in winter (here November to April) comparing satellite-derived products and IABP/C buoy data: (a) OSISAF, (b) CERSAT, (c) KIMURA, and (d) NSIDC.

spatial pattern or time series are still not possible due to the very sparse spatial coverage of the in situ data. Therefore, we limit our attention to differences of monthly mean drift speed between the satellite products and the buoy data.

Figure 18 shows scatter plots of ice drift from the satellite derived products and IABP/C in winter. Correlation coefficients are 0.91 (OSISAF), 0.67 (CERSAT), 0.86 (KIMURA), and 0.94 (NSIDC), respectively. OSISAF and NSIDC give relatively small root mean square error (hereafter RMSE, OSISAF: 0.93 cm s^{-1} , NSIDC: 1.01 cm s^{-1}), whereas KIMURA and CERSAT give larger RMSEs (KIMURA: 1.36 cm s^{-1} , CERSAT: 1.86 cm s^{-1}). The error of the drift speed is generally dependent on the magnitude of the drift speed (Figure 19). OSISAF and CERSAT show similar distribution of error dependence: an almost linear increase from $0.7\text{--}0.9 \text{ cm s}^{-1}$ error in the $0\text{--}1 \text{ cm s}^{-1}$ bin to $1.1\text{--}1.6 \text{ cm s}^{-1}$ error in the $5\text{--}6 \text{ cm s}^{-1}$ bin. KIMURA shows nearly constant error of about 1 cm s^{-1} from the 0 to 5 cm s^{-1} bins. NSIDC shows linear increase of error from 0.6 cm s^{-1} ($0\text{--}1 \text{ cm s}^{-1}$ bin) to 1.2 cm s^{-1} ($5\text{--}6 \text{ cm s}^{-1}$ bin), which is the smallest error of the four products. Note that the ice motion field of NSIDC is obtained from merging satellite and buoy data, and that it is thus not surprising that NSIDC shows the smallest mismatch to buoy drift. On the other hand, as shown in ice drift speed (Figures 11 and 12) and ice drift curl (Figures 16 and 17), other products give better correspondence to the interpolated buoy data (IABP/D) than NSIDC.

In summer (May to October), both KIMURA and NSIDC give lower correlation coefficients (KIMURA: 0.75, NSIDC: 0.87) and larger RMSE (KIMURA: 1.65 cm s^{-1} , NSIDC: 1.30 cm s^{-1}) compared to the winter data

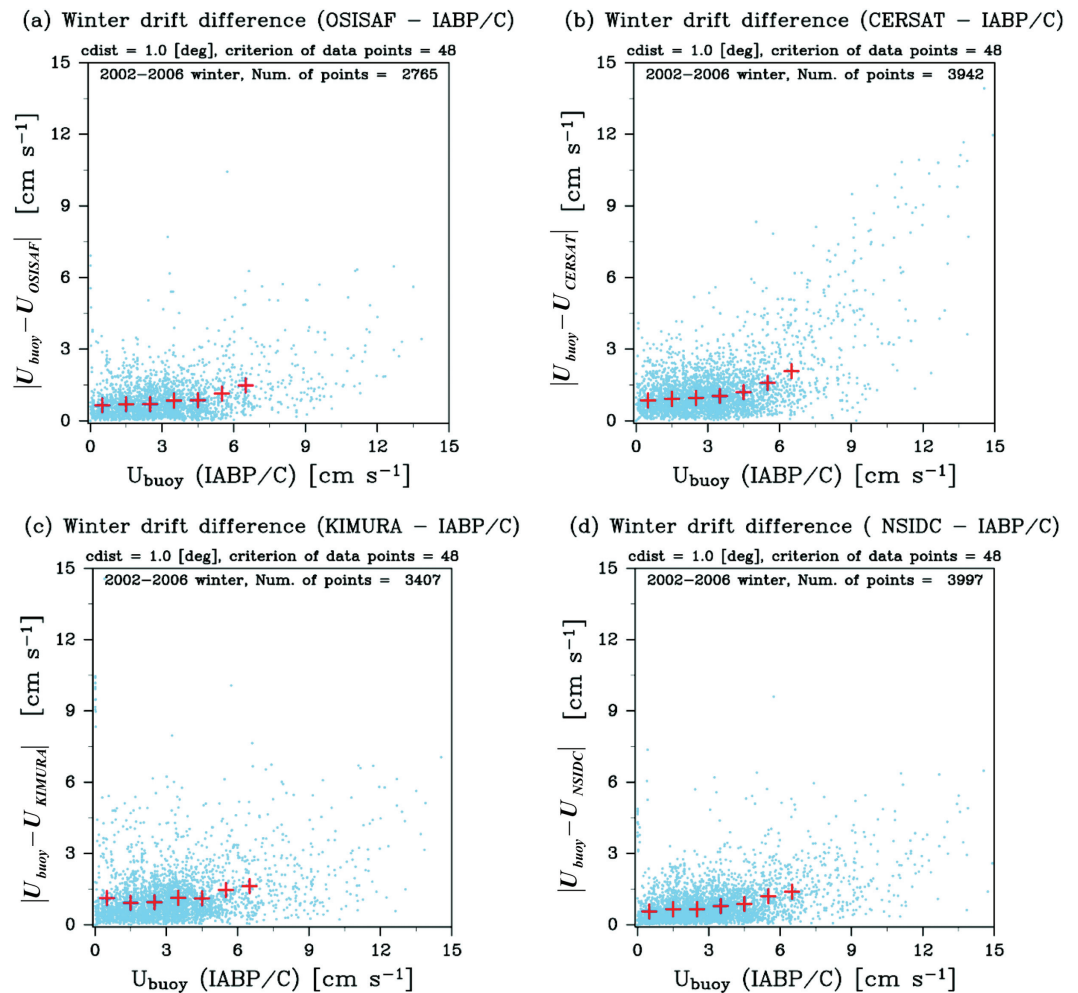


Figure 19. Scatter plot of ice drift difference between satellite-derived and IABP/C buoy data as a function of buoy drift speed: (a) OSISAF, (b) CERSAT, (c) KIMURA, and (d) NSIDC. Ice drift data in winter (November to April) from 2002 to 2006 were used to plot the points. Each light-blue point denotes difference of ice drift at a certain grid point. The red crosses denote the mean difference of ice drift in a certain bin (1.0 cm s⁻¹ width) of IABP/C buoy drift speed.

(Figure 20). The magnitude of the error of both KIMURA and NSIDC is dependent on the IABP/C drift speed (Figure 21). KIMURA exhibits a slight tendency to slower speeds compared to buoy drift speed, whereas NSIDC exhibits a clear tendency to slower speeds, although NSIDC shows generally a weaker scatter than KIMURA (Figure 20). The scatter of NSIDC is weaker because the cokriging method uses the in situ buoy drift. The tendency toward slower speeds is presumably due to discrepancy between the ice-drift vectors estimated from the satellite images and those obtained from buoy observation.

3.5. Uncertainty Estimates

In this subsection, we deduce uncertainty estimates for the monthly mean ice drift for the respective products, which can be directly applied for model validation and/or data assimilation. For the uncertainty estimates, we utilize ice concentration and ice drift speed of the winter season. It has been shown that the difference of ice drift vectors between the products is large (small) in low (high) ice concentration area (section 3.1), and that the ice drift difference between products and buoys (IABP/C) is large (small) for high (low) drift speed (section 3.4). We first closely examine the relations between the differences of the ice drift vectors and its relation to ice concentration and ice-drift speed, and second estimate uncertainties as a function of ice concentration and drift speed. At the end of this subsection we show an example of combined uncertainty maps for the respective products.

For the uncertainty estimates, we measure the ice drift difference by the magnitude of the difference of two vectors, i.e., $|\mathbf{U}_{diff}| = |\mathbf{U}_{product1} - \mathbf{U}_{product2}|$. It should be noted that this definition does not directly

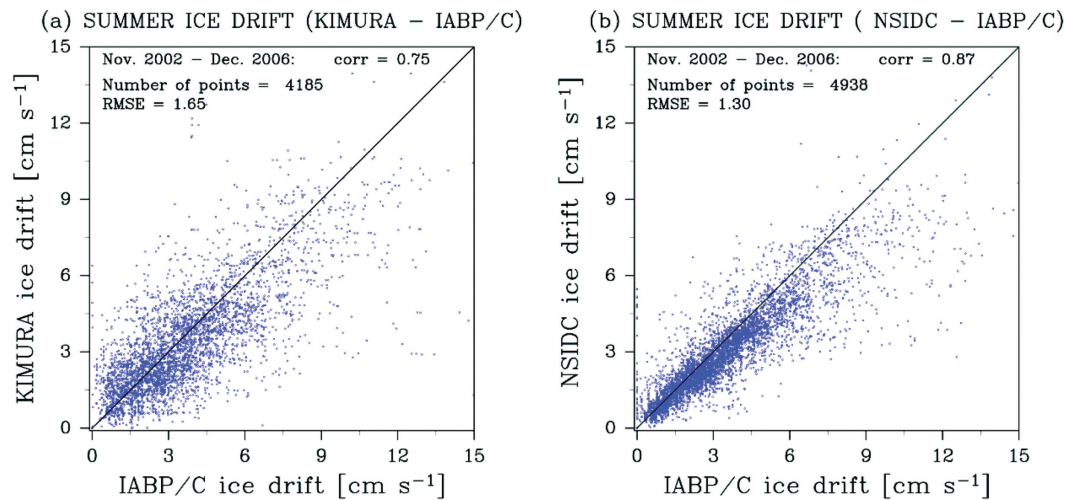


Figure 20. Scatter plot of ice drift speed in summer (May to October) from 2003 to 2006, comparing satellite-derived products and IABP/C buoy data: (a) KIMURA and (b) NSIDC. The solid black line corresponds to a line showing an exact coincidence of the drift speed between the two data.

measure the difference of ice drift speed, $|\mathbf{U}_{product1}| - |\mathbf{U}_{product2}|$, nor the difference of drift direction, $\cos^{-1}(\mathbf{U}_{product1} \cdot \mathbf{U}_{product2}) / (|\mathbf{U}_{product1}| |\mathbf{U}_{product2}|)$, but implicitly measures both of them. Advantages of the presented measure are (1) the uncertainties can be quantified by one scalar variable, $|\mathbf{U}_{diff}|$, (2) we do not need to assume that the uncertainty is anisotropic, and (3) estimated uncertainties can be directly applied to a different coordinate system without vector rotation.

To quantify the relation between ice-drift difference and ice concentration, we examine the functional dependence of ice-drift difference on ice concentration (Figure 22a). We classified the difference of the ice-drift vectors in 15 ice-concentration bins and plotted the distributions of the difference in the respective bins (The interval of the bins is not linear in order to secure sufficient number of data points. See the interval of the points in Figure 22b.). Figure 22a shows three examples of ice-drift difference distributions in different ice-concentration bins for the difference between CERSAT and NSIDC. As clearly seen in this figure, the shapes of the probability density functions differ between the bins, whereas all the distributions can be reasonably approximated by lognormal distributions (dashed lines in Figure 22a);

$$f_a(\mathbf{U}_{diff}) = \frac{1}{\sqrt{2\pi}\sigma_a|\mathbf{U}_{diff}(a)|} \exp\left[-\frac{(\log|\mathbf{U}_{diff}(a)| - \mu_a)^2}{2\sigma_a^2}\right], \quad (4)$$

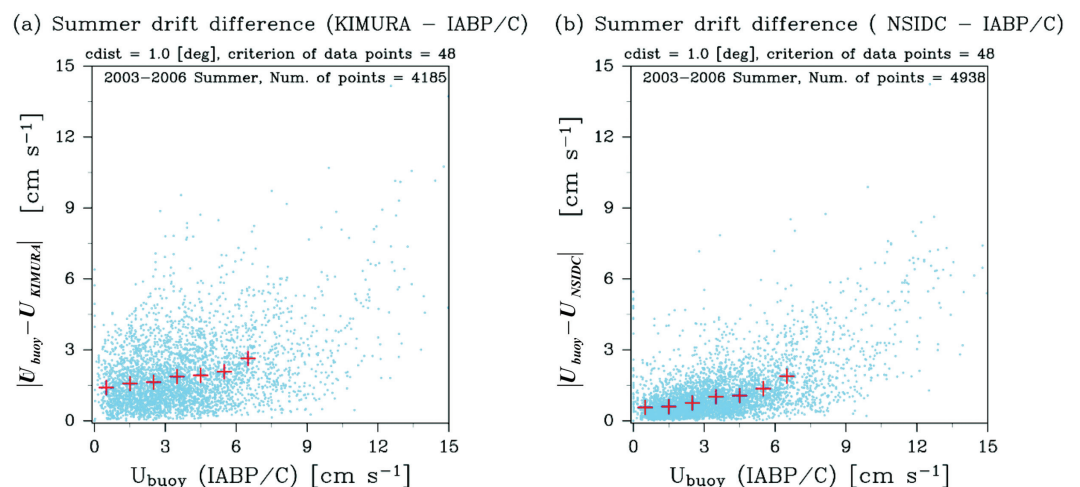


Figure 21. The same as Figure 19, but for summer (May to October): (a) KIMURA and (b) NSIDC.

where $\mathbf{U}_{diff}(a)$ is the ice-drift difference in a selected bin 'a,' and σ_a and μ_a are the parameters of the lognormal distributions calculated from the distributions in the respective bins. We deduced that such a lognormal approximation can be applied to all bins with ice concentrations larger than 80% for any combination of the products except for any combination where OSISAF is involved (not shown), because generally OSISAF does not give ice drifts in low ice concentrations areas (see Figures 7a–7c). The mean ($E_a(\mathbf{U}_{diff})$) and standard deviation ($\sqrt{V_a(\mathbf{U}_{diff})}$) of the lognormal distributions are given by

$$E_a(\mathbf{U}_{diff}) = \exp\left[\mu_a + \frac{\sigma_a^2}{2}\right] \tag{5}$$

and

$$\sqrt{V_a(\mathbf{U}_{diff})} = \sqrt{\exp[2\mu_a + 2\sigma_a^2] - \exp[2\mu_a + \sigma_a^2]}, \tag{6}$$

respectively. We calculate means and standard deviations in the respective bins for all combination of the products (Figures 22b and 22c). Figure 22b shows that the mean difference between the ice drifts is sufficiently small in high ice concentration (97%>) areas, whereas the difference increases as the concentration decreases. Particularly, the combination of CERSAT and KIMURA gives the largest difference exceeding 4 cm s⁻¹ for ice concentrations lower than 92%. The standard deviations (Figure 22c) also exhibit a similar tendency, i.e., smaller (larger) standard deviations in the higher (lower) ice concentration areas. We define the uncertainty of the ice drift in a certain area with a given ice concentration as the sum of the mean difference (also called bias, Figure 22b) and the standard deviation (Figure 22c) of the lognormal distribution of the corresponding bin.

We perform a similar analysis to estimate uncertainties with respect to the magnitude of the ice-drift speed (Figure 23). We utilize the relation found in Figure 19—the larger the drift speed the larger the deviation from monthly mean IABP/C drift. For all grid points where monthly mean IABP/C drift is available, we calculate the difference from IABP/C and classified the data into six ice-drift speed bins with constant width (1 cm s⁻¹, drift speeds exceeding 5 cm s⁻¹ are classified to the largest bin). The bins are defined with respect to the drift speed of the respective products (not with respect to the IABP/C drift speed as in Figure 19) in order to relate the uncertainties to the drift of the products. Figure 23a shows examples of distributions of the ice drift error of three different bins for KIMURA. Although the number of available data is limited, again, the distributions clearly show a lognormal distribution (dashed lines in Figure 23a). A lognormal distribution gives a reasonable approximation for all bins and for all products (not shown) and we calculate means and standard deviations of the lognormal functions corresponding to the respective bins for all products (Figures 23b and 23c). The mean error is generally smaller for slower drift speed and gradually increases toward higher drift speed (Figure 23b). This tendency is also common to the standard deviation shown in Figure 24c. With the help of the empirical functions shown in Figures 23b and 23c, we define the uncertainty of ice drift for a certain ice-drift speed as the sum of the mean error (Figure 23b) and the standard deviation (Figure 22c) as in the case of the dependence of the error on the ice concentration.

Figure 24 shows exemplarily the spatial patterns of the components of the uncertainties depending on the ice concentration (Figure 24e) and the ice-drift speed (Figure 24f) for OSISAF for January 2003. Figures 24a–24d correspond to the uncertainties associated with Figures 22b, 22c, 23b, and 24c, respectively. For the uncertainties associated with the ice concentration (Figures 24a and 24b), we averaged the three different estimates coming from the three possible combinations of the products (i.e., we put the same weight to all products and assumed that the errors of the respective products are not correlated). Since we could not estimate uncertainties for ice concentration lower than 90% for the combinations with OSISAF, the uncertainty of the 90–91% ice-concentration bin is applied to the areas whose ice concentration is lower than 90%. In Figures 24a and 24b, we can see relatively large uncertainty north of Fram Strait in line with the low ice concentration in this area (Figure 24e). Figures 24c and 24d also exhibit slightly larger uncertainty north of Alaska, the central Arctic, and north of Fram Strait corresponding to the relatively large drift speeds in these areas (Figure 24f).

Figure 25 summarizes the estimates of the uncertainties for all products exemplarily for January 2003. To combine the uncertainties associated with ice concentration and ice drift speed, we took the larger values at each locations to define the overall uncertainties, i.e., the uncertainty ε at a certain location is given by

$$\varepsilon = \text{Max} \left(\overline{E_a(\mathbf{U}_{diff})} + \sqrt{\overline{V_a(\mathbf{U}_{diff})}}, E_s(\mathbf{U}_{bias}) + \sqrt{V_s(\mathbf{U}_{bias})} \right). \quad (7)$$

where $E_s(\mathbf{U}_{bias})$ and $\sqrt{V_s(\mathbf{U}_{bias})}$ are the mean bias and the standard deviation in the corresponding ice-drift speed bin. All products exhibit large uncertainties in low ice concentration (Figure 24e) and large drift speed (Figures 3a–3d) areas consistent with the comparison results shown in subsections 3.1, 3.2, and 3.4. OSISAF and NSIDC exhibits relatively small uncertainties in vast regions of the central Arctic because of their relatively small uncertainties in high ice concentration (Figure 22b and 22c) and slow drift speed areas (Figures 23b and 23c), while CERSAT exhibits slightly larger uncertainties for the corresponding area due to the relatively large uncertainties for slow ice drift speed (Figures 23b and 23c). KIMURA also exhibits slightly larger uncertainties relative to OSISAF and NSIDC because of the large uncertainties coming from the difference from CERSAT.

4. Summary and Discussion

4.1. Summary

We made an intercomparison of four different Arctic Ocean low-resolution ice-drift products derived from satellite observations, and also examined their differences to buoy drift data. The products are inferred from different sensors with different time and space scales, and different motion-tracking algorithms. To standardize the temporal representation of the data and to provide practical information for use in model validation, we processed the drift data to monthly mean vectors. The comparison mainly focuses on differences of winter ice drift because of the limitation of seasonal coverage of the products. The purpose of the present comparison is not to rank the performance of the products but to provide practical information to data users regarding the differences between the products and to provide uncertainty estimates based on the statistics of the differences. From our point of view, all the products are practical and useful for model validation and data assimilation, if the uncertainty and error statistics are given in a proper way. The present intercomparison intends to provide some additional aspects on this issue.

The comparison of drift patterns show that the differences among the products are not spatially uniform, but are emphasized in some specific regions such as southern part of the Canadian Basin, the Greenland Sea, the Kara Sea, and the Barents Sea, whereas the differences are relatively small in the central Arctic. The strength of differences are related to the ice concentration and the ice thickness. In high ice concentration areas (99–100%), the mean differences of drift vectors are small (0.6–0.8 cm s⁻¹) and they gradually increase to 0.9–4.4 cm s⁻¹ in 89–90% ice concentration areas. In thicker ice areas (4.5–5.0 m), mean differences of the drift range from 0.5 to 0.8 cm s⁻¹ depending on a combination of the products, whereas those in thinner ice areas (0.5–1 m) range from 0.7 to 1.9 cm s⁻¹. Direct comparisons with the buoy-based drift speeds indicate that the error also depends on the drift speed. In all products, faster ice drift speed generally gives larger errors; the error is roughly less than 1 cm s⁻¹ for ice drift speeds slower than 3 cm s⁻¹ while the error exceeds 1.6 cm s⁻¹ for ice drifts larger than 5 cm s⁻¹.

For examinations of drift speed, we adopt spatial and temporal scales proposed by Rampal et al. [2009] to separate between the mean and fluctuations. Based on their analysis, we divided ice drift between mean (5 months averaged and 400 km spatially filtered drift) and monthly fluctuations from the mean. Regarding the modal distribution of mean drift speed, all products show similar distribution of the bulk occurrences in the range of 1–3 cm s⁻¹, but different features regarding the tails toward the large velocities. For the fluctuating part of the velocity, all products show similar distribution of frequencies from 0 to about 5 cm s⁻¹, and slightly different shapes of tails for the drift speed higher than 7 cm s⁻¹. The analysis with this scale separation revealed that the differences between the products are evident for large drift speeds in the mean field. The spatially domain-wide and temporally over the whole time period averaged winter drift speeds range from 1.8 to 2.0 cm s⁻¹, and those of winter fluctuation range from 2.5 to 2.8 cm s⁻¹, which correspond to a maximal difference of 10% between the products. The RMSDs between the products range from 0.7 to 2.6 cm s⁻¹, which is slightly larger than RMSEs obtained from direct comparison of satellite products and buoy data (0.9–1.9 cm s⁻¹) and is considerably larger than the interpolation error of the monthly mean IABP/C drift (0.68 cm s⁻¹, see section 2.6).

A comparison of transpolar drift speed shows that the mean difference of the drift speed is 0.32 cm s⁻¹ (2002–2006 winter average), which leads to 13% difference of ice mass transport across the central Arctic (if we ignore variation of ice thickness). Another remarkable point is the difference of ice drift curl. The spatial

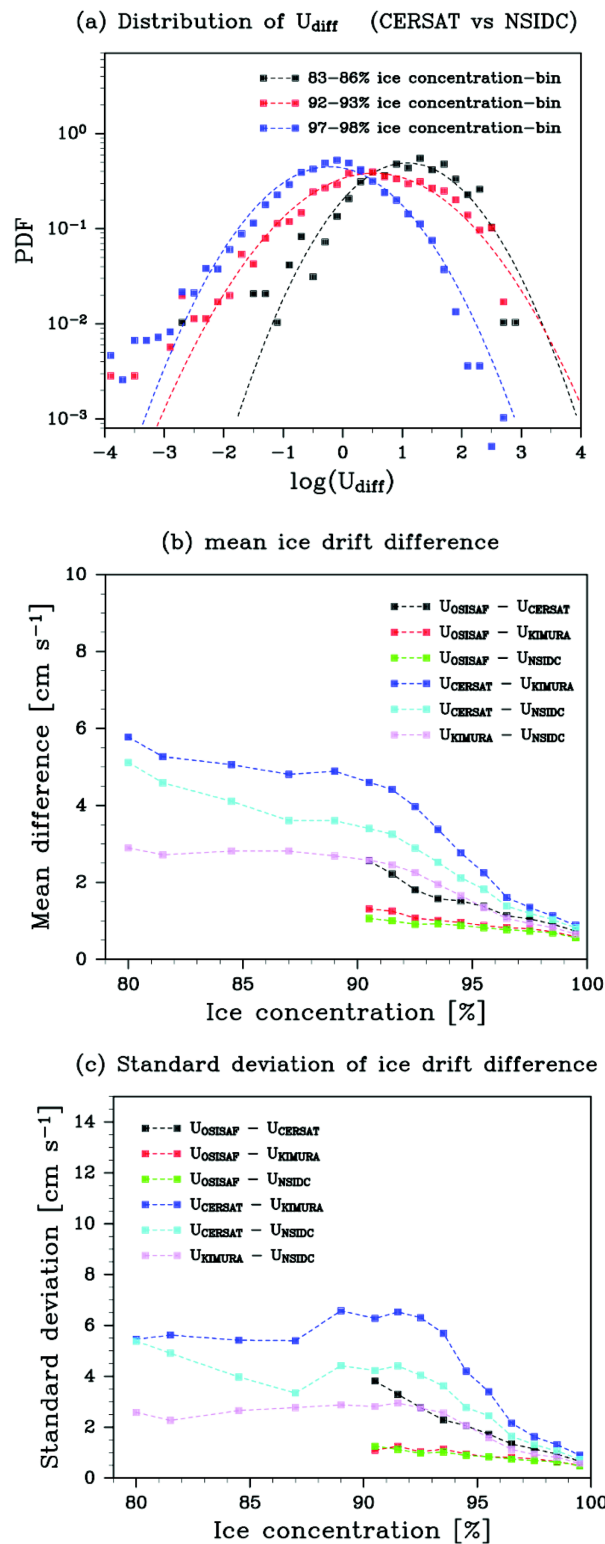


Figure 22. Examples of ice drift difference distribution in three different ice-concentration bins (a) (black: 83–86%, red: 92–93%, blue: 97–98%) obtained from the difference between CERSAT and NSIDC. The squares denote distribution of the difference, while the dashed lines denote the corresponding lognormal distribution. (b) Mean ice drift difference and (c) standard deviation of ice drift difference in respective ice-concentration bins estimated from the corresponding lognormal distribution.

patterns of the curl exhibit different features in small scale and also different spatial scales of fluctuations, which lead to remarkable difference of total amount of negative and positive curls, even though the sum of them agrees well. Such difference may lead to a different dynamical balance of modeled sea ice and resultant ocean circulation, when the different products are applied for data assimilation. The ice drift curl calculated from the products revealed that the temporal average of ice drift curl in winter differs by 18% on average, and the difference in the Amerasian Basin comes up to 24% at maximum. This indicates that downward Ekman pumping estimated from the ice motion differs by more than 20% of the total Ekman pumping (if we assume a constant ice-ocean drag coefficient). Since both of these features are significant measures to evaluate the performance of coupled Arctic sea ice-ocean models, the models validated from different products may have a similar magnitude of differences.

Based on the present comparison results, we estimated uncertainties of monthly mean ice drift for the respective products. The uncertainties are based on the difference between the products and difference from the monthly mean buoy drift. We examined functional forms of the distribution of the difference in relation to ice concentration, and found that the distributions can be reasonably approximated by a lognormal function whose parameters depend on ice concentration and combination of the products. For ice drift speed, we performed a similar analysis and found that the distributions of

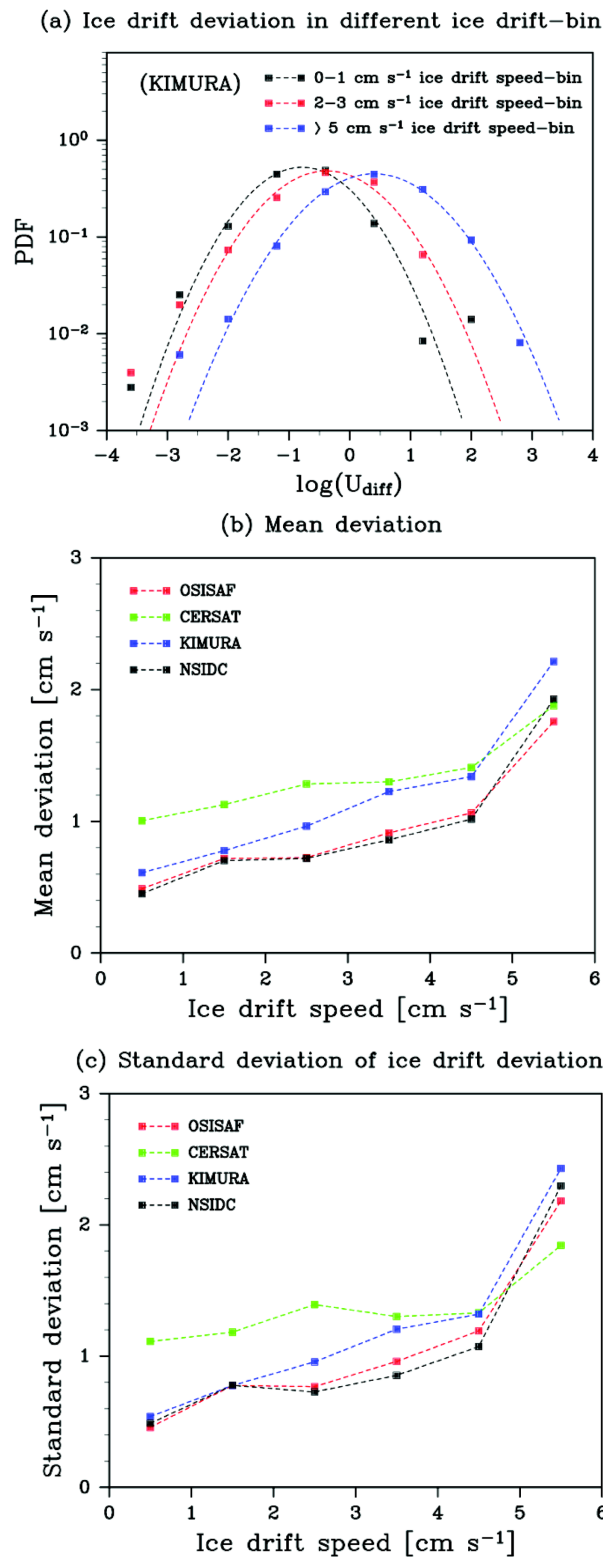


Figure 23. (a) Examples of distributions of ice drift deviation from monthly mean IABP/C drift in three ice drift speed bins (black: 0–1 cm s⁻¹, red: 2–3 cm s⁻¹, blue: > 5 cm s⁻¹) for KIMURA. (b) Mean deviation and (c) standard deviation from monthly mean IABP/C drift estimated from the corresponding lognormal distribution.

the bias can also be approximated by lognormal distributions which allow to estimate uncertainties. We defined the total uncertainty of a certain drift vector as the maximum of the sum of the mean difference (mean bias) and the standard deviation associated with ice concentration and drift speed, respectively. The estimated uncertainty maps reasonably reflect the difference between the products in relation to ice concentration and bias from buoy drift in relation to drift speed. OSISAF and NSIDC exhibit relatively small uncertainties compared to CERSAT and KIMURA. The relatively large uncertainty of CERSAT is partly due to the slightly larger bias in slow drift speed compared to the other products and also due to the large differences to KIMURA in low ice concentration areas. KIMURA exhibits slightly larger uncertainties compared to OSISAF and NSIDC, due to the large difference to CERSAT in low ice concentration areas. The extrapolation used in KIMURA (see section 2.3) affects the uncertainties close to the coasts. Application of the estimated uncertainties to a data assimilation will be presented in forthcoming papers.

4.2. Discussion

The main differences outlined by our comparison stem from, (1) the type of satellite imaging data used as input, (2) the ice motion tracking algorithm implemented, (3) the extent to which interpolation techniques are used, and (4) the time and space scales. Table 1 summarizes the approaches and input satellite data used for each data set. Both the CERSAT and NSIDC data sets implement the MCC algorithm, which leads to

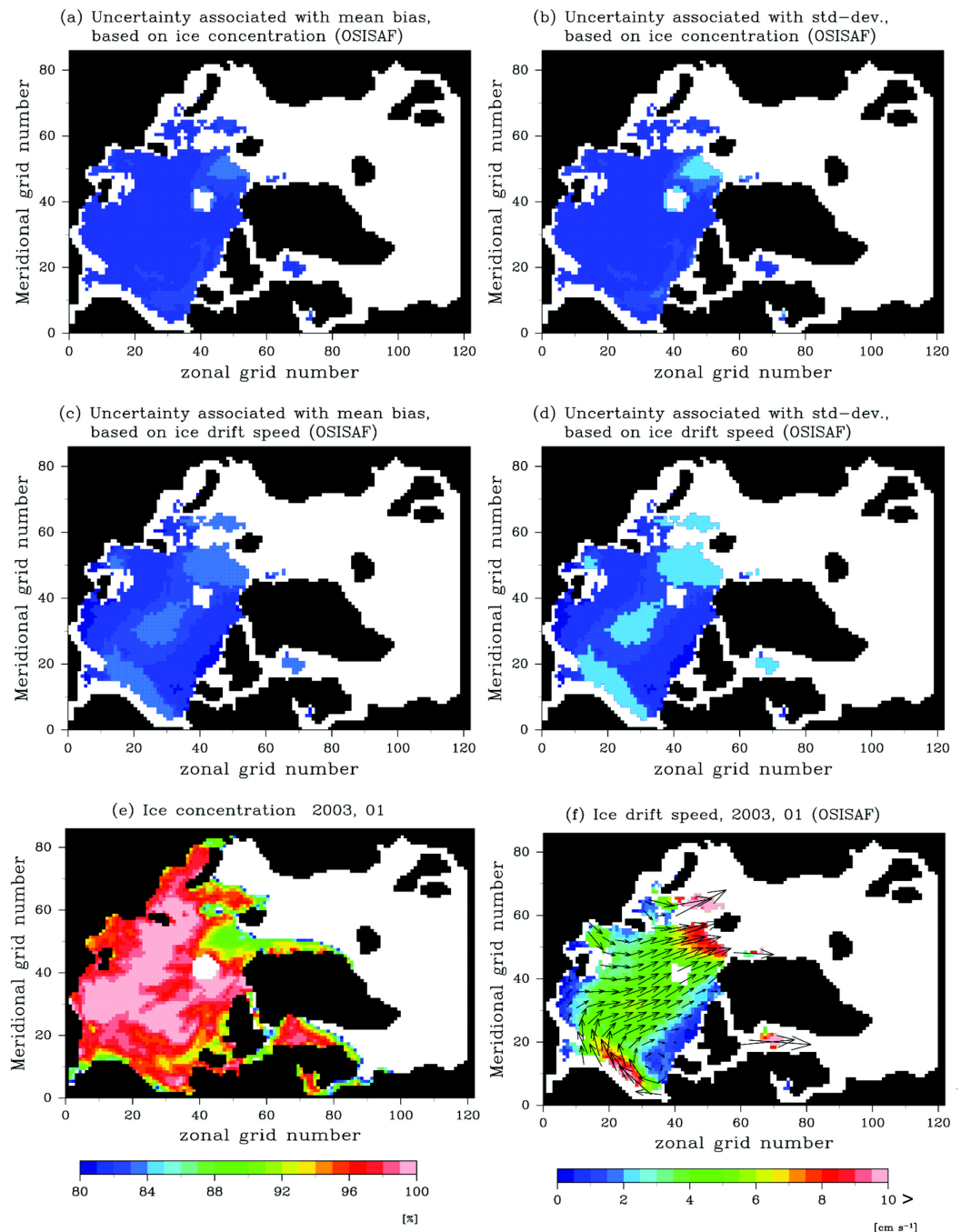


Figure 24. Uncertainty estimates of the ice drift vectors based on ice concentration (a), (b) and ice drift speed (c), (d), and corresponding ice concentration (e) and ice drift speed (f) in January, 2003. The uncertainty maps are (a) uncertainties associated with the mean difference from other products related to the ice concentration, (b) uncertainties associated with the standard deviation of the difference related to the ice concentration, (c) uncertainties associated with the mean bias from IABP/C drift speed, and (d) uncertainties associated with the standard deviation of the bias from IABP/C drift speed. For the Figures 24a–d, the same color table as for Figure 24(f) is used. The uncertainty estimates are examples for the OSISAF product.

pronounced quantization noise (section 3.2) on a daily basis. NSIDC reduces the noise by applying cokriging with several other ice motion estimates. A large part of this daily-basis noise is additionally smoothed by the computation of monthly averaged drift in our study. Both OSISAF and KIMURA implement some sort of enhanced MCC algorithm, and thus do not suffer from the quantization noise. In addition to the algorithm approach, the choice of sensors and channels is of importance.

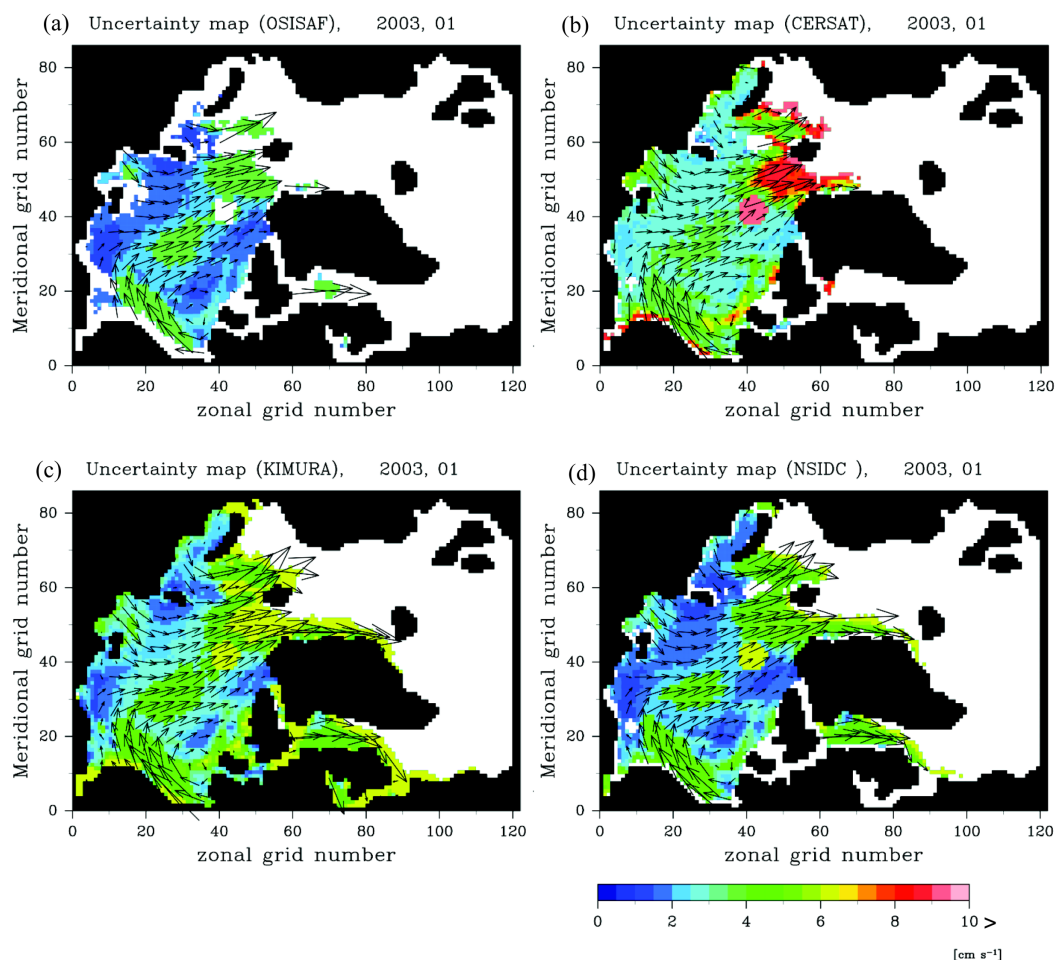


Figure 25. Uncertainty maps of ice drift vectors for (a) OSISAF, (b) CERSAT, (c) KIMURA, and (d) NSIDC in January 2003. The vector field shows the sea ice drift while the color shows the magnitude of the uncertainty vectors. The magnitude of the ice drift can be found in Figure 3 and the corresponding ice concentration can be found in Figure 24.

By processing the 37 GHz channels of the AMSR-E instrument, the OSISAF data set aims at an accuracy which is more stable with season, mostly stable over the whole winter, since the 37 GHz imagery is less prone to atmospheric noise than the high-frequency (89 GHz) channels [Lavergne *et al.*, 2010]. The latter are used by KIMURA during winter. Higher atmospheric water content over sea ice in early autumn and late spring can indeed reduce the accuracy of ice motion based on high-frequency channels [Kwok *et al.*, 1998]. However, at the core of winter (December to March), these channels offer stable enough imaging of the ice surface, and are particularly interesting for motion tracking thanks to their finer spatial resolution.

The NSIDC product uses both frequencies for SSM/I and AMSR-E, so is also prone to some error due to weather effects in the high-frequency channels. A spatial coherence technique is utilized to filter out motion vectors that are influenced by these effects. The most accurate motions are achieved during winter, when the cold, dry atmosphere contributes the minimum interference. Ice motion tends to be slower during this period, enabling the tracking method to incur less error than in spring and autumn, when ice conditions change more rapidly. Summertime error exceeds that of winter, due in part to surface melt, which affects the passive microwave identification of ice parcels. The largest error is found in the fall, which is likely due to formation of new ice [Meier *et al.*, 2000].

CERSAT products are based on the merging of microwave passive and active sensors, which has several benefits: this enables to extend the time window (C-band scatterometer is useful to detect motion at freeze period because it is less sensitive to surface wetness), increase the reliability of the inferred vector (the combination provides more reliable vectors than each individual ones since each drift is inferred from independent measurement), and, increase notably the number of available vectors (by 20–30%), in particular at early fall and spring [Girard-Arduin and Ezraty, 2012].

Based on our uncertainty estimates in section 3.4, for validation of sea ice models we recommend to use the OSISAF product, which only provides ice displacement in areas where the uncertainty is comparatively low, leading to an exclusion of data for example in low ice concentration area. Since defining an uncertainty of respective drift vectors as a function of ice concentration and ice drift speed for model validation imposes substantial additional work to the modelers, the product which provides only low-uncertainty ice drift is favorable for the users. This argument is also applicable to simple data assimilation (hereafter DA) techniques such as nudging. For all DA techniques which do not take into account a relative weighting of observations as a function of uncertainty, it is favorable to use a product which disregards data with high uncertainty. For advanced DA techniques on the other hand, which minimize a cost function defined by the norm of the model-data misfit, normalized by the uncertainty (such as Kalman filter, 4-Dimensional variational data assimilation; 4-DVar, etc.), all of the investigated products are possible to be used, as long as the uncertainty of the data products are taken into account (for example calculated with a method as the one described in this study). In such a case a product which covers as much of the ice covered area as possible is preferable; however, which would narrow the best choice to the products from KIMURA and NSIDC.

Sea ice drift products are delivered with limited estimates of the uncertainties, which are provided as constant values in space and time in most cases. Better uncertainties are, however, indispensable for a quantitative model validation or for data assimilation. The uncertainty estimates provided in this study makes it possible to assess modeled ice drift depending the uncertainty of the respective drift vectors. This is a big advantage not only for DA but also for model validation. With such uncertainty estimates, modelers can appropriately constrain their modeled ice drift in a low-uncertainty area, while, at the same time, can avoid to overconstrain their model results in high-uncertainty area. This advantage is particularly relevant to advanced DA in which a combination of different types of data is applied (i.e., a combination of ocean data, ice concentration, ice thickness, and etc.). For DA with such a combination of several data products, uncertainties of the respective data are essential to obtain a consistent contribution from the respective data. It is therefore of paramount importance that ice motion producers further investigate such ice motion uncertainty algorithms and deliver maps of uncertainties along with their drift products, on a daily basis. For the time being, and for the purpose of providing uncertainties on a monthly basis, the differences among the various products exposed here can be parameterized in an uncertainty model for the ice drift.

For further assessment of uncertainty of the products, high-resolution ice drift vectors derived from Synthetic Aperture Radar (SAR) [e.g., MyOcean; Karvonen, 2012; RGPS; Kwok and Cunningham, 2003, Kwok et al, 2008] can be applied. As shown in this study, the differences of the low-resolution products are significantly large in low ice concentration areas. Since it is demanding task to increase the number of buoys in this low ice concentration areas, a validation of the products by SAR products will offer further assessment of their uncertainties in low ice concentration areas and may contribute to improve the motion-tracking algorithms used in the products.

In its most recent "satellite supplement" of the Global Climate Observing System (GCOS) Requirement Document [Global Climate Observing System (GCOS), 2011], the World Meteorological Organization states that the target requirement accuracy for the sea ice drift variable is 1 km day⁻¹ on weekly basis [GCOS, 2011, p. 52]. Considering that we documented here RMSD of easily 4 cm s⁻¹ (3.5 km day⁻¹) on a monthly basis, we can only conclude that more work should be put into deriving satellite-based products for climate applications, to narrow down the differences between the products, which hopefully means to narrow down also the errors.

Appendix A

The statistical significance of the difference between the individual ice thickness-bins is tested by the following procedure, where $|U_{diff.}(m)|$ is the difference of ice drift speed between two products in m -th

Table A1. t-Statistics for Difference of Mean Ice Drift Difference, $(|U_{diff.}(m)| - |U_{diff.}(m+n)|)$, for Different Distance of Ice Thickness-Bins, n , with $m = 1^a$

Combination of Products	n = 1	n = 2	n = 3	n = 4	n = 5	n = 6	n = 7
OSISAF—CERSAT	0.74	0.73	-0.03	0.17	0.47	0.95	0.84
OSISAF—KIMURA	0.67	0.51	0.49	0.33	0.31	0.51	0.78
OSISAF—NSIDC2	0.58	0.97	0.63	0.39	0.37	0.93	1.05
CERSAT—KIMURA	<u>2.81</u>	<u>2.40</u>	<u>2.19</u>	<u>2.40</u>	<u>2.33</u>	<u>3.59</u>	<u>3.89</u>
CERSAT—NSIDC2	<u>1.91</u>	<u>(1.48)</u>	<u>(1.44)</u>	<u>(1.63)</u>	1.17	<u>2.62</u>	<u>2.93</u>
KIMURA—NSIDC2	<u>1.83</u>	<u>1.66</u>	<u>(1.60)</u>	<u>(1.49)</u>	<u>1.76</u>	<u>2.53</u>	<u>2.83</u>

^aThe t-statistic values which reject the null hypothesis H_0 with 95% (90%) confidence level are underlined. See text for details.

ice-thickness bin. The ice-thickness bins of 0.5 m width are numbered by $m = 1, 2, \dots, 9$ for the 1.0–1.5 m, 1.5–2.0 m, ..., 5.0–5.5 m bins, respectively.

1. Examine the distribution of $|U_{diff.}(m)|$ to find the functional form of the probability density function (PDF) in the respective ice-thickness bins.

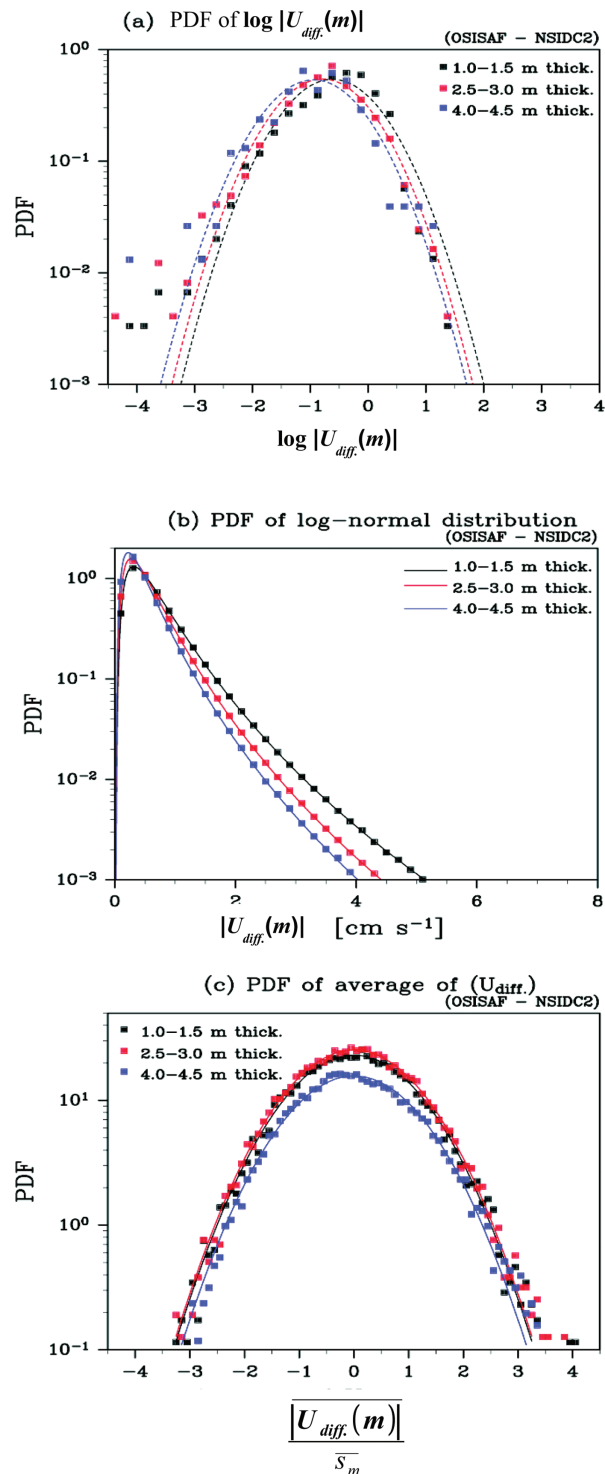


Figure A1. An example of (a) the distribution of the monthly mean ice drift difference, $|U_{diff.}(m)|$, (b) the lognormal distributions estimated from the $|U_{diff.}(m)|$ distribution (lines) and the PDFs of random numbers used for Monte-Carlo simulations (dots), and (c) PDF of $\overline{|U_{diff.}(m)|}$ estimated from the Monte-Carlo simulations. Dots and lines with black, red, and blue denote the PDFs for ice-thickness bins of 1.0–1.5 m, 2.5–3.0 m, and 4.0–4.5 m, respectively. The plots show exemplarily results for the difference between OSISAF and NSIDC.

2. Estimate the distribution of $\overline{|\mathbf{U}_{diff.}(m)|}$ with the given number of data samples, N_m , in the respective ice-thickness bins by Monte-Carlo simulations, where the functional forms of $|\mathbf{U}_{diff.}(m)|$ are given by step 1.
3. Do Welch's test [Welch, 1947] to examine the statistical significance of the difference between $\overline{|\mathbf{U}_{diff.}(m)|}$ and $\overline{|\mathbf{U}_{diff.}(m+n)|}$ with given numbers of data samples N_m and N_{m+n} by using the PDFs estimated in step 2, where n is a positive integer measuring the distance between the ice-thickness bins.

The above test is performed for all combinations of the products.

Figure A1 (a) shows three examples of $|\mathbf{U}_{diff.}(m)|$ obtained from the monthly mean ice drift differences between OSISAF and NSIDC. In this figure, ice drift differences of three ice thickness-bins ($m = 1, 4, \text{ and } 7$, corresponding to ice thickness bins of 1.0–1.5 m, 2.5–3.0 m, and 4.0–4.5 m, respectively) are plotted by squares. We found that the distributions can be approximated by a lognormal distribution,

$$PDF_{|\mathbf{U}_{diff.}(m)|} = \frac{1}{\sqrt{2\pi}s_m|\mathbf{U}_{diff.}(m)|} \exp \left[\frac{-(\log |\mathbf{U}_{diff.}(m)| - \mu_m)^2}{2s_m^2} \right], \quad (A1)$$

where the distribution parameters, s_m^2 and μ_m , are calculated from the distributions of $|\mathbf{U}_{diff.}(m)|$ in the respective ice-thickness bins (dashed lines in Figure A1a). By using the functional form of (1), Monte-Carlo simulations are performed to estimate distribution of $\overline{|\mathbf{U}_{diff.}(m)|}$ for the respective bins. In this simulations, we generate 10,000 sets of N_m times random numbers for the respective bins, whose PDF is given by the corresponding lognormal distribution (Figure A1b), and estimate the functional form of the mean ice drift difference distribution for each bin (Figure A1c). We found that the distributions of $\overline{|\mathbf{U}_{diff.}(m)|}$ can be approximated by Gaussian distributions,

$$PDF_{\overline{|\mathbf{U}_{diff.}(m)|}} = \frac{1}{\sqrt{2\pi}\overline{s}_m\overline{|\mathbf{U}_{diff.}(m)|}} \exp \left[\frac{-\left(\overline{|\mathbf{U}_{diff.}(m)|} - \mu_m\right)^2}{2\overline{s}_m^2} \right], \quad (A2)$$

whose variance \overline{s}_m^2 is a function of the number of available data samples, N_m (Figure A1c). Since the distributions of $\overline{|\mathbf{U}_{diff.}(m)|}$ with the given numbers of data samples can be approximated by a Gaussian distribution, we can define a two-sample t -statistic for the difference of population means as,

$$t = \frac{\left(\overline{|\mathbf{U}_{diff.}(m)|} - \overline{|\mathbf{U}_{diff.}(m+n)|}\right)}{\sqrt{\overline{s}_m^2 + \overline{s}_{m+n}^2}}, \quad (A3)$$

Where \overline{s}_m^2 and \overline{s}_{m+n}^2 are the sample variance of $\overline{|\mathbf{U}_{diff.}(m)|}$ and $\overline{|\mathbf{U}_{diff.}(m+n)|}$ estimated from the Monte-Carlo simulations. To examine the statistical significance of the difference of the means, we adopt a Welch's test [Welch, 1947]. Welch's test is a statistical test for the difference of the population means with unknown (different) variances of the two populations. According to Welch [1947], the degree of freedom of equation (A3) can be approximated by that of a $t(v^*)$ -distribution, where v^* is the closest integer of v ;

$$v = \frac{(\overline{s}_m^2 + \overline{s}_{m+n}^2)^2}{\frac{(\overline{s}_m^2)^2}{N_m - 1} + \frac{(\overline{s}_{m+n}^2)^2}{N_{m+n} - 1}}. \quad (A4)$$

We test the null hypothesis $H_0: \left(\overline{|\mathbf{U}_{diff.}(m)|} = \overline{|\mathbf{U}_{diff.}(m+n)|}\right)$ against an alternative hypothesis $H_1: \left(\overline{|\mathbf{U}_{diff.}(m)|} > \overline{|\mathbf{U}_{diff.}(m+n)|}\right)$ with n being the distance between the bins. Table A1 summarizes the t -statistics obtained from different n values ($m = 1$) for combinations of the products. The t -statistic values which reject the null hypothesis H_0 with 95% (90%) confidence level are underlined. Except for the combinations including OSISAF, we find significant differences with 95% confidence level for 1–2 m thickness differences.

References

- Colony, R., and A. S. Thorndike (1984), An estimate of the mean field of Arctic sea ice motion, *J. Geophys. Res.*, *89*(C6), 10623–10629, doi: 10.1029/JC089iC06p10623.
- Colony, R. L., and I. Rigor (1989), Arctic Ocean Buoy Program Data Report for 1 January 1986 to 31 December 1986, *Tech. Memo., APL-UW TM 6-89*, Appl. Phys. Lab., Univ. of Wash, Seattle.

Acknowledgments

Funding by the Helmholtz Climate Initiative REKLIM (Regional Climate Change), a joint research project of the Helmholtz Association of German research centers (HGF) is gratefully acknowledged. This work has partly been supported by the European Commission as part of the FP7 project ACCESS—Arctic Climate Change, Economy and Society (Proj. Nr., 265863). We also would like to express our gratitude towards the German Federal Ministry of Education and Research for the support of the project "Beiträge des Nordpolarmeers zu Veränderungen des Nordatlantiks" (03F0443D). The authors express their gratitude for all the data provider; the ice drift products were provided by EUMETSAT OSI SAF (OSI-405: ftp://osisaf.met.no/archive/ice/drift_lr/), Ifremer/CERSAT (<ftp://ftp.ifremer.fr/ifremer/cersat/products/gridded/psi-drift/data/arctic/>), N. Kimura at the University of Tokyo and NSIDC (<http://nsidc.org/data/nsidc-0116.html/>); the ice tethered buoy data were provided by IABP, University of Washington (<http://iabp.apl.washington.edu/data.html>); the ice concentration and thickness data were provided by OSI SAF (OSI-409:<ftp://osisaf.met.no/preprocessed/ice/conc/v1/>) and by R. Kwok at Jet Propulsion Laboratory (<http://rkwok.jpl.nasa.gov/icesat/download.html>), respectively. The GFD-DENNOU library was used to draw the figures. Finally, the authors deeply appreciate the thorough reviews by two anonymous reviewers, which substantially contributed to the improvement of this study.

- Dai, M., T. E. Arbetter, and W. N. Meier (2006), Data assimilation of sea—ice motion vectors: Sensitivity to the parameterization of sea—ice strength, *Ann. Glaciol.*, *44*, 357–360.
- Eastwood, S., K. R. Larsen, T. Lavergne, E. Nielsen, and R. Tonboe (2010), *Global Sea Ice Concentration Reprocessing Product User Manual, Product OSI-409*, The EUMETSAT Network of Satellite Appl. Fac.
- Emery, W. J., C. W. Fowler, and J. A. Maslanik (1997), Satellite-derived maps of Arctic and Antarctic sea ice motion: 1988 to 1994, *Geophys. Res. Lett.*, *24*(8), 897–900, doi:10.1029/97GL00755.
- Fowler, C. (2003), *Polar Pathfinder Daily 25 km EASE-Grid Sea Ice Motion Vectors (daily and mean gridded field)*, NASA DAAC at the Natl. Snow and Ice Data Cent., Boulder, Colo.
- Fowler, C., W. Emery, and M. Tschudi (2013), *Polar Pathfinder Daily 25 km EASE-Grid Sea Ice Motion Vectors. Version 2. (daily and mean gridded field)*, NASA DAAC at the Natl. Snow and Ice Data Cent., Boulder, Colo., USA.
- Gandin, L. S. (1965), The objective analysis of meteorological fields, Leningrad, *Hydrometeorol. Publ. House, 1963*, Engl. Transl., Isr. Program for Sci. Transl., Jerusalem.
- Global Climate Observing System (2011), *Systematic Observation Requirements for Satellite-based Products for Climate Supplemental Details to the Satellite-Based Component of the Implementation Plan for the Global Observing System for Climate in Support of the UNFCCC: 2011 Update*, World Meteorological Organization, Geneva, Switzerland.
- Girard-Ardhuin, F., and R. Ezraty (2012), Enhanced Arctic sea ice drift estimation merging radiometer and scatterometer data, *IEEE Trans. Geosci. Remote Sens.*, *50*(7), 2639–2648, doi:10.1109/TGRS.2012.2184124.
- Hwang, B., and T. Lavergne (2010), *Validation and Comparison of OSI SAF Low and Medium Resolution and IFREMER/Cersat Sea Ice Drift Products, CDOP-SG06-VS02*, The EUMETSAT Network of Satellite Appl. Fac.
- Isaaks, E., and R. M. Srivastava (1989), *An Introduction to Applied Geostatistics*, Oxford Univ. Press, N. Y.
- Karvonen, J. (2012), Operational SAR-based sea ice drift monitoring over the Baltic Sea, *Ocean Sci.*, *8*, 473–483, doi:10.5194/os-8-473-2012.
- Kauker, F., T. Kaminski, M. Karcher, R. Giering, R. Gerdes, and M. Voßbeck (2009), Adjoint analysis of the 2007 all time Arctic sea-ice minimum, *Geophys. Res. Lett.*, *36*, L03707, doi:10.1029/2008GL036323.
- Kimura, N., and M. Wakatsuchi (2000), Relationship between sea: Ice motion and geostrophic wind in the northern hemisphere, *Geophys. Res. Lett.*, *27*(22), 3735–3738, doi:10.1029/2000GL011495.
- Kimura, N., and M. Wakatsuchi (2004), Increase and decrease of sea ice area in the Sea of Okhotsk: Ice production in coastal polynyas and dynamical thickening in convergence zones, *J. Geophys. Res.*, *109*, C09S03, doi:10.1029/2003JC002196.
- Kimura, N., A. Nishimura, Y. Tanaka, and H. Yamaguchi (2013), Influence of winter sea ice motion on summer ice cover in the Arctic, *Polar Res.*, *32*, 20193 pp., doi:10.3402/polar.v32i0.20193.
- Kreyscher, M., M. Harder, P. Lemke, and G. M. Flato (2000), Results of the Sea Ice Model Intercomparison Project: Evaluation of sea ice rheology schemes for use in climate simulations, *J. Geophys. Res.*, *105*(C5), 11299–11320, doi:10.1029/1999JC000016.
- Kwok, R., and G. F. Cunningham (2003), Sub-daily sea ice motion and deformation from RADARSAT observations, *Geophys. Res. Lett.*, *30*(23), 2218, doi:10.1029/2003GL018723.
- Kwok, R., and G. F. Cunningham (2008), ICESat over Arctic sea ice: Estimation of snow depth and ice thickness, *J. Geophys. Res.*, *113*, C08010, doi:10.1029/2008JC004753.
- Kwok, R., A. Schweiger, D. A. Rothrock, S. Pang, and C. Kottmeier (1998), Sea ice motion from satellite passive microwave imagery assessed with ERS SAR and buoy motions, *J. Geophys. Res.*, *103*(C4), 8191–8214, doi:10.1029/97JC03334.
- Kwok, R., G. F. Cunningham, H. J. Zwally, and D. Yi (2007), Ice, Cloud, and land Elevation Satellite (ICESat) over Arctic sea ice: Retrieval of freeboard, *J. Geophys. Res.*, *112*, C12013, doi:10.1029/2006JC003978.
- Kwok, R., E. C. Hunke, W. Maslowski, D. Menemenlis, and J. Zhang (2008), Variability of sea ice simulations assessed with RGPS kinematics, *J. Geophys. Res.*, *113*, C11012, doi:10.1029/2008JC004783.
- Kwok, R., G. F. Cunningham, M. Wensnahan, I. Rigor, H. J. Zwally, and D. Yi (2009), Thinning and volume loss of the Arctic Ocean sea ice cover: 2003–2008, *J. Geophys. Res.*, *114*, C07005, doi:10.1029/2009JC005312.
- Lavergne, T., and S. Eastwood (2010), *Low Resolution Sea Ice Drift Product User's Manual, GBL LR SID—OSI 405*, The EUMETSAT Network of Satellite Appl. Fac.
- Lavergne, T., S. Eastwood, Z. Teffah, H. Schyberg, and L.-A. Breivik (2010), Sea ice motion from low-resolution satellite sensors: An alternative method and its validation in the Arctic, *J. Geophys. Res.*, *115*, C10032, doi:10.1029/2009JC005958.
- Martin, T., and R. Gerdes (2007), Sea ice drift variability in Arctic Ocean Model Intercomparison Project models and observation, *J. Geophys. Res.*, *112*, C04S10, doi:10.1029/2006JC003617.
- Meier, W. N., J. A. Maslanik, and C. W. Fowler (2000), Error analysis and assimilation of remotely sensed ice motion within an Arctic sea ice model, *J. Geophys. Res.*, *105*(C2), 3339–3356, doi:10.1029/1999JC900268.
- Menke, W. (1989), *Geophysical data analysis: Discrete inverse theory (revised ed.)*, Int. Geophys. Ser., vol. 45, Academic, San Diego, Calif.
- Miller, P. A., S. W. Laxon, D. L. Feltham, and D. J. Gresswell (2006), Optimization of a sea ice model using Basinwide observations of arctic sea ice thickness, extent, and velocity, *J. Clim.*, *19*(7), 1089–1108.
- Nguyen, A. T., D. Menemenlis, and R. Kwok (2011), Arctic ice-ocean simulation with optimized model parameters: Approach and assessment, *J. Geophys. Res.*, *116*, C04025, doi:10.1029/2010JC006573.
- Ortmeyer, M., and I. G. Rigor (2004), International Arctic Buoy Program data report 2003, *Tech. Memo. APL-UW TM 2–04*, Appl. Phys. Lab., Univ. of Wash., Seattle, Wash.
- Proshutinsky, A. Y., and M. A. Johnson (1997), Two circulation regimes of the wind-driven Arctic Ocean, *J. Geophys. Res.*, *102*(C6), 12493–12514, doi:10.1029/97JC00738.
- Proshutinsky, A., R. Krishfield, M.-L. Timmermans, J. Toole, E. Carmack, F. McLaughlin, W. J. Williams, S. Zimmermann, M. Itoh, and K. Shimada (2009), Beaufort Gyre freshwater reservoir: State and variability from observations, *J. Geophys. Res.*, *114*, C00A10, doi:10.1029/2008JC0054104.
- Rampal, P., J. Weiss, D. Marsan, and M. Bourgoin (2009), Arctic sea ice velocity field: General circulation and turbulent-like fluctuations, *J. Geophys. Res.*, *114*, C10014, doi:10.1029/2008JC005227.
- Rollenhagen, K., R. Timmermann, T. Janjić, J. Schröter, and S. Danilov (2009), Assimilation of sea ice motion in a finite-element sea ice model, *J. Geophys. Res.*, *114*, C05007, doi:10.1029/2008JC005067.
- Rozman, P., J. A. Hölemann, T. Krumpen, R. Gerdes, C. Köberle, T. Lavergne, S. Adams, and F. Girard-Ardhuin (2011), Validating satellite derived and modelled sea-ice drift in the Laptev Sea with in situ measurements from the winter of 2007/08, *Polar Res.*, *30*, 7218, doi:10.3402/polar.v30i0.7218.
- Sakov, P., F. Counillon, L. Bertino, K. A. Lisæter, P. R. Oke, and A. Korabely (2012), TOPAZ4: An ocean-sea ice data assimilation system for the North Atlantic and Arctic, *Ocean Sci.*, *8*, 633–656, doi:10.5194/os-8-633-2012.

- Stark, J. D., J. Ridley, M. Martin, and A. Hines (2008), Sea ice concentration and motion assimilation in a sea ice–ocean model, *J. Geophys. Res.*, *113*, C05S91, doi:10.1029/2007JC004224.
- Sumata, H., F. Kauker, R. Gerdes, C. Köberle, and M. Karcher (2013), A comparison between gradient descent and stochastic approaches for parameter optimization of a sea ice model, *Ocean Sci.*, *9*, 609–630, doi:10.5194/os-9-609-2013.
- Thorndike, A. S., and L. Colony (1982), Sea ice motion in response to geostrophic winds, *J. Geophys. Res.*, *87*(C8), 5845–5852, doi:10.1029/JC087iC08p05845.
- Thorndike, A. S., L. Colony, and E. Munoz (1983), *Arctic Ocean Buoy Program: Data Report 1 January 1982–31 December 1982*, Polar Sci. Cent., Univ. of Wash, Seattle, Wash.
- Tremblay, L.-B., and M. Hakakian (2006), Estimating the sea ice compressive strength from satellite-derived sea ice drift and NCEP reanalysis data, *J. Phys. Oceanogr.*, *36*(11), 2165–2172.
- Tschudi, M.A., C. Fowler, J. A. Maslanik, and J. Stroeve (2010), Tracking the movement and changing surface characteristics of Arctic sea ice, *IEEE J. Selected Topics Earth Obs. Remote Sens.*, *3*(4), pp. 536–540, doi:10.1109/JSTARS.2010.2048305.
- Welch, B. L. (1947), The generalization of ‘Student’s’ problem when several different population variances are involved. *Biometrika*, *34*(1-2), 28–35, doi:10.1093/biomet/34.1-2.28.
- Zygmuntowska, M., P. Rampal, N. Ivanova, and L. H. Smedsrud (2013), Uncertainties in Arctic sea ice thickness and volume: New estimates and implications for trends, *Cryosphere*, *7*, 5051–5095, doi:10.5194/tcd-7-5051-2013.

Erratum

In the originally published version of this article, in Figures 22–25, the calculation of the standard deviations of the log-transformed ice drift difference were erroneous. This miscalculation affects subsequent analyses and the presented ice drift uncertainties. Additionally, there was a typesetting error in equation (2). These errors have been corrected, and this version may be considered the authoritative version of record.